Universität Zürich[UZH]

Benefits of Minimizing the Vertex Detector Material Budget at the FCC-ee

Bachelor Thesis
of the University of Zurich

Author:

Leila Freitag

Supervised by:

Dr. Armin Ilg
and
Prof. Dr. Ben Kilminster

January 2023
Physics Institute

CERN-THESIS-2023-013
01/02/2023

Abstract

With the discovery of the Higgs boson, the Standard Model of particle physics is complete. Yet, many questions about the nature of particles remain unanswered by it. The FCC-ee is a proposed lepton collider that will provide high precision measurements of Standard Model particle properties, which can reveal the tiniest deviations from Standard Model predictions. The vertex detector, which lies closest to the interaction point in a detector, is responsible for the reconstruction of the vertex, which is the position where the particle interaction occurs. Precise location of these vertices is for example important for the identification of heavy jets as well as tau leptons, which propagate a small distance from the primary vertex and decay at a secondary vertex. To accomplish this, the vertex detector should minimize the amount of material added to the detector in order to reduce the multiple scattering that particles experience. One concept for a detector at the FCC-ee is the IDEA detector. This Bachelor thesis investigates the benefits of minimizing the material budget of the IDEA vertex detector. Such a detector is based on the curved sensor technology developed for ALICE ITS3, where wafer-scale DMAPS sensors with a thickness of 20 to 40 μm can be bent to form detector layers. In order to study the vertex detector performance, the metrics of impact parameter resolution, flight distance resolution, and secondary vertex resolution are investigated. To this end, DELPHES is used to perform fast simulation of detector response to $Z \to \mu^+\mu^-$ events, particle gun muons, and strange B meson decays. It was found that reducing the thickness of the three innermost vertex detector layers from 280 μm to 30 μm shows significant improvement in impact parameter resolution (the fit parameter b that describes the multiple scattering contribution is reduced by about 30%), as well as in flight distance resolution (about 6% improvement) and secondary vertex resolution (about 20% improvement). Even only reducing the thickness of the first vertex detector layer, which is most easily achievable since it is small enough to be constructed with one single silicon wafer, already improves the secondary vertex resolution by about 6%. Minimizing the thickness of the eight vertex disc layers yields a small additional improvement in performance, especially in the forward region, but is less influential than reducing the thickness of the inner barrel layers.

Contents

Introduction

High energy physics aims to determine the fundamental particles that make up matter, and to study their interactions. The current understanding is described in the Standard Model of particle physics, which describes the fundamental forces of nature excluding gravity. It contains two kinds of particles; the *fermions* are the particles that make up matter, and the *bosons* mediate the interactions between particles. Fermions can be further divided into *leptons* and *quarks*. There are three generations of leptons, with the later generations having a higher mass. The lightest generation of leptons contains the *electron*, and its corresponding electron neutrino. The next generations of leptons contain two heavier siblings of the electron, the *muon* (μ) and the *tau* (τ), and their respective neutrinos. Neutrinos are chargeless and massless, while the other leptons have charge $-e$, where e is the elementary charge. Analogous to the leptons, the quarks also come in three generations, each containing an *up*- and *down*-type quark. The former include the *up* (u), *charm* (c) and *top* (t) quarks, which have charge $\frac{2}{3}e$. The latter include the *down* (d), *strange* (s), and *bottom* (b) quarks, which have charge $-\frac{1}{3}e$. Quarks can combine to form composite particles, or *hadrons*; more specifically, a hadron made of two quarks is called a *meson*, and one consisting of three quarks is called a *baryon*. Quarks within hadrons such as the proton (uud), are held together by the strong interaction, where the mediator particle is the *gluon*. In fact, quarks interact via all three forces described by the Standard Model. The electron and its heavier siblings experience the electroweak interaction, which is a unified description of the electromagnetic and weak interaction, mediated by the *photon*, the Z boson, and the W bosons. The neutrinos experience only the weak interaction, which is for example responsible for β-decay and nuclear fusion in stars. Lastly there is the *Higgs* boson, which gives mass to the quarks, charged leptons, and Z and W bosons. Also, every fermion has an *antiparticle* with the same properties as the fermion except with the opposite charge. In particle physics experiments, particles are collided at high energies to look for evidence of new particles, or deviations from theory predictions.

In the early- to mid-1900s, before man-made particle accelerators could reach high energies, cosmic rays were used to study subatomic particles. These high energy particles (usually protons or nuclei) originate from the sun or elsewhere in the universe, and produce showers of secondary particles when they hit earth's atmosphere. The positron (antiparticle of the electron) and the muon were discovered through cosmic ray studies in 1932 and 1936 respectively. Then, with the ability to accelerate beams of particles, scientists could conduct *fixed target experiments* by aiming the beam at a stationary target. The antiproton was discovered at the Bevatron in 1955, which accelerated protons into a fixed target. An essential quantity when thinking about accelerators is the *center of mass energy*, which is the energy that is made available for the creation of new parti-

cles in a particle collision. In fixed target collisions, the center of mass energy is only a fraction of the impinging particle's energy, as the second colliding particle is at rest. To reach higher center of mass energies, *collider experiments* with head-on collisions of two beams of particles are better suited, since the center of mass energy is the sum of the two beam energies.

Additionally, particle colliders can be *linear* or *circular*. An advantage of circular colliders is being able to reuse the particles in a bunch that do not collide in future collisions, while in linear colliders these are lost. However, circular colliders must use magnetic fields to keep the accelerated particles on the circular trajectory. The energy that these particles can reach is limited by the field strength of available bending magnets, and by energy losses due to bremsstrahlung. Furthermore, different particles can be used in collider experiments. Using protons allows new energy ranges to be explored, since their mass allows them to be accelerated to higher energies without significant energy loss due to bremsstrahlung. However, because it is the quarks and gluons within the proton that interact in a collision, there is a lot of *pile-up*, which is the presence of many inelastic proton-proton interactions that obscure the hard collisions that are of interest. This means that the interesting physics needs to be found among a huge number of collisions. The total cross section is many orders of magnitude greater than the cross section of processes of interest! The problem of pile-up is much less severe in electron-positron (e^+e^-) colliders. Unlike protons, electrons are elementary particles, and the collision energy is fixed by the beam energy, making them good for precision measurements. Historically, advances in particle physics have been made with both types of collisions. Figure 1 shows colliders since the 1960s.

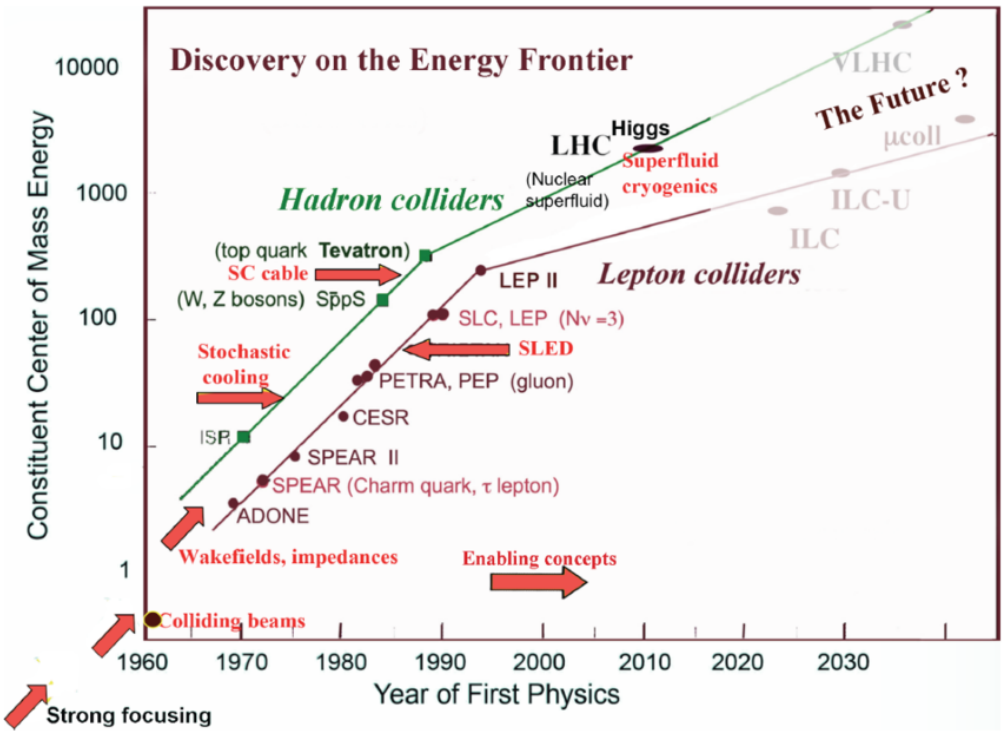

Figure 1: Livingston plot of the effective collision energy of both hadron (green) and electron–positron (dark red) colliders, as a function of completion date. Also indicated by red arrows are the innovations in accelerator technology that enabled progress [1].

Electron-positron collisions can also provide insight on particles of higher mass that are not explicitly produced in the collision due to the center of mass energy not being high enough. For example, precise measurements of the cross section of $e^+e^- \to f\overline{f}$ (electron-positron annihilation to two fermions) can be sensitive to the top quark and Higgs boson, since these contribute to the cross section in quantum loop corrections as illustrated in Figure 2. In fact, the top quark mass could be predicted using these high precision fermion pair production cross section measurements done at the Large Electron Positron collider (LEP), for which the Large Hadron Collider (LHC) tunnel was originally built. The top quark was later discovered at the Tevatron.

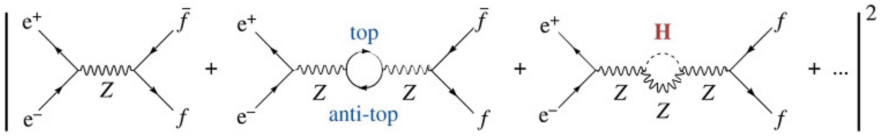

Figure 2: Feynman diagrams showing how the calculation of the cross section of electron-positron annihilation to two fermions involves perturbative expansion with higher order quantum loop corrections [2].

The Higgs boson, discovered at the LHC in 2012, was the final particle predicted in the Standard Model. Now considered complete, what is left to do is to continue testing the its predictions to see if experimental findings agree with theory within the theoretical uncertainties. There are phenomena that the Standard Model cannot explain, including the observed matter-antimatter asymmetry, the existence of dark matter, an explanation of gravity on a quantum level, and the origin of non-zero neutrino masses. Collider experiments so far have shown consistency with Standard Model predictions, and indicate that new physics might be at a much higher energy scale or have very weak couplings. Either way, large improvements are needed in precision measurements to probe these possibilities.

For the next large particle collider after the High-Luminosity LHC, electron-positron collider concepts are favored. There is no guaranteed new particle discovery on the horizon, which means that precision measurements should be employed to reveal tiny cracks of the Standard Model. There are several proposed designs for e^+e^- colliders currently being developed and explored. The most prominent ones are the following four:

- The Compact Linear Collider (CLIC)[3]: 11 to 50 km linear accelerator at CERN
- The International Linear Collider (ILC)[4]: ∼20 km long accelerator in Japan, focusing on studying the Higgs boson.
- The Circular Electron Positron Collider (CEPC)[5]: ∼100 km circumference tunnel in China, to study the Z boson, W boson, Higgs boson, and possibly the top quark.
- The Future e^+e^- Circular Collider (FCC-ee)[2]: ∼100 km circumference tunnel at CERN, to study the Z boson, W boson, Higgs boson, and the top quark.

The instantaneous luminosity $\mathcal{L}$ is a quantity that is related to the collision rate at a particle accelerator. It is useful to describe the performance of the accelerator, since higher luminosity means more statistics. It is also the proportionality factor that relates the measured rate in a detector R to the cross section σ of a physics process. Integrating the instantaneous luminosity over time gives the instantaneous luminosity L, which is then related to the number of collisions N. Written explicitly, the relation is:

$$R = \mathcal{L} \cdot \sigma, \quad \text{or} \quad N = L \cdot \sigma, \quad \text{where} \quad L = \int \mathcal{L}\, dt. \tag{1}$$

The luminosities expected to be delivered by these four e^+e^- collider projects are shown in Figure 3. The FCC-ee will be the focus of this thesis, and is discussed in more detail in the following Chapter 1.

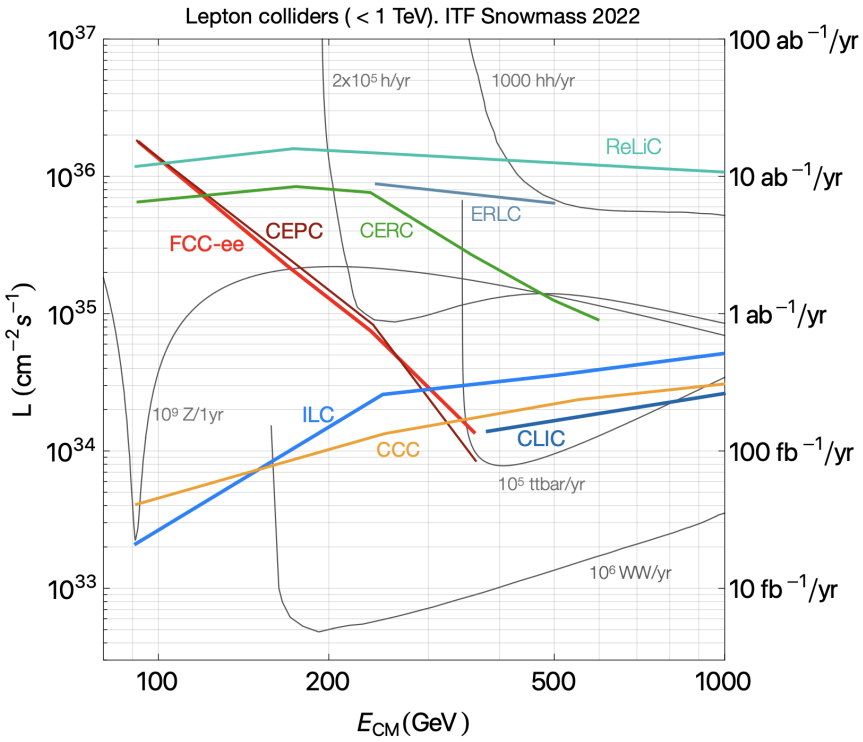

Figure 3: Expected luminosities to be delivered by proposed e^+e^- collider projects (FCC-ee in red, CEPC in dark red, ILC in blue, CLIC in dark blue) as a function of center of mass energy, taken from Reference [6]. The y-axis on the left hand side is the instantaneous luminosity, and the right hand side shows the integrated luminosity per 10^7 seconds, which is the typical operation time for an accelerator in one year.

Chapter 1

The Future Circular Collider Project

The Future Circular Collider (FCC) is a proposed particle collider to succeed the High-Luminosity phase of the LHC in the 2040's. The FCC ring would have a circumference of about 100 km – a massive collider even compared to the LHC's 27 km. The FCC would serve to expand particle physics knowledge on both the energy and intensity frontiers, having the opportunity to house a setup for both electron-positron collisions (FCC-ee [2]) and hadron (proton-proton or heavy ion) collisions (FCC-hh [7]) in the same tunnel concurrently. The plan is to start with FCC-ee and then follow with FCC-hh in the 2060's or 2070's. The focus of this thesis will be the electron-positron collider FCC-ee.

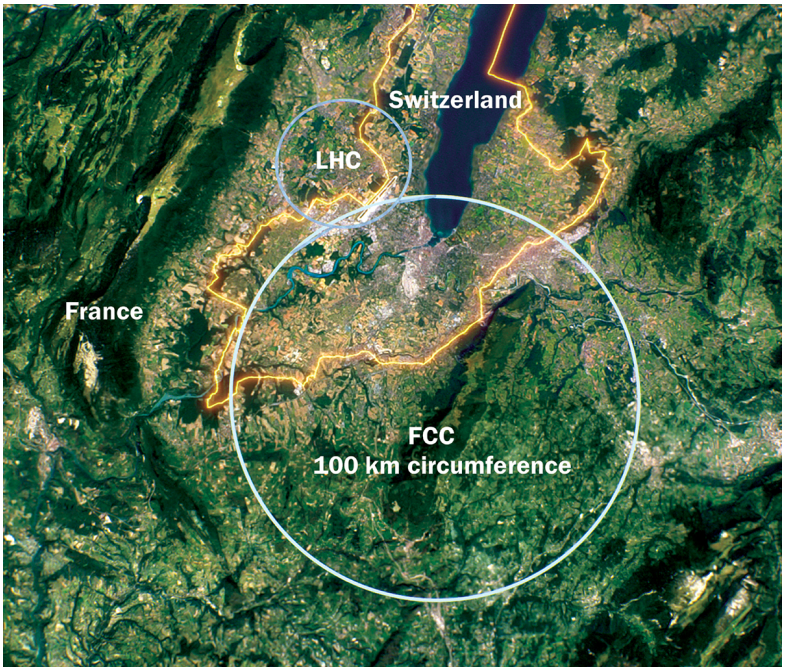

Figure 1.1: Proposed sketch of the 100 km FCC ring in the Geneva area with the LHC for scale [8].

1.1 FCC-ee Physics Potential

There are four planned phases of operation at the FCC-ee; e^+e^- collisions at the Z pole (91 GeV), at the WW threshold (161 GeV), as a Higgs factory (240 GeV), and at the $t\bar{t}$ threshold (340–365 GeV). The integrated luminosities planned to be achieved in these four modes are illustrated in Figure 1.2.

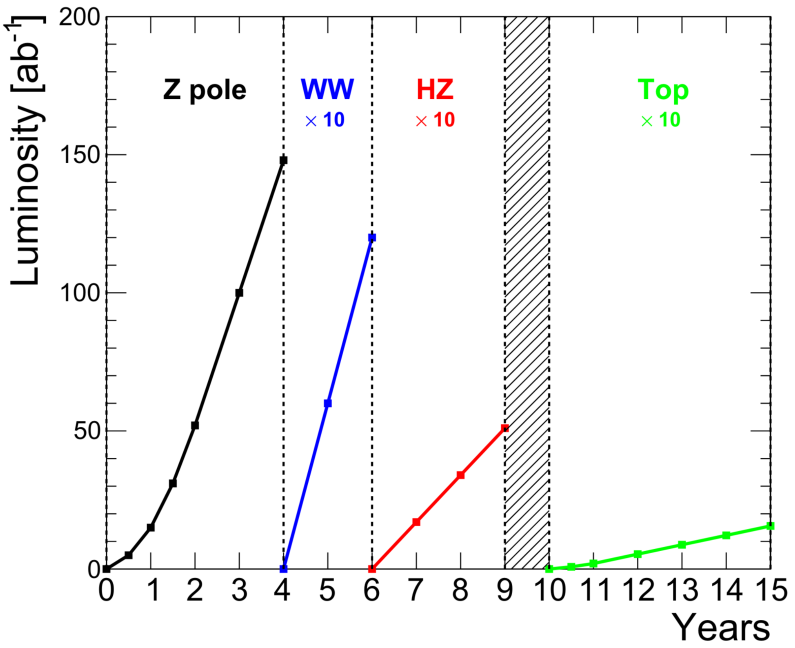

Figure 1.2: Evolution of the integrated luminosity for the four phases of operation of FCC-ee over time. Operation at the highest center of mass energy of the $t\bar{t}$ threshold (green) requires reconfiguration of the collider, which will occur during a year-long shutdown [2].

The FCC-ee, as a high luminosity lepton collider with clean collisions and precise detectors, is ideal for precision measurements. It will be able to perform measurements of the properties of the four Standard Model particles with highest mass (the W boson, Z boson, Higgs boson, and the top quark) with unprecedented precision. Furthermore it provides the possibility to detect rare processes and look for small deviations from the Standard Model.

1.2 FCC-ee Detector Requirements

A particle detector needs to be able to reconstruct particle collisions with the highest efficiency possible. This means reconstructing the four-momenta of the products of the interaction well, and having accurate particle identification. Particles are detected by exploiting their interactions with matter, i.e. the material of the detector. The key components of a traditional particle detector are the vertex detector, tracker, magnet, calorimeters, and muon detectors. Figure 1.3 illustrates how different particle types leave different signatures in the various components. This information can be used for particle identification.

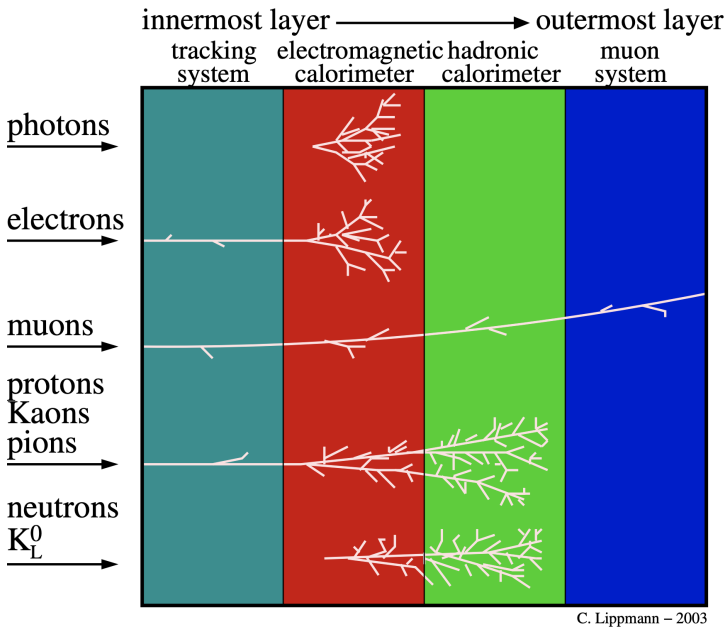

Figure 1.3: Components of a traditional particle detector, from innermost position to outermost layer [9]. Different types of particles leave different track signatures in the components, and the presence of a magnetic field curves the tracks of charged particles.

The nominal interaction point is where the two beams of particles are brought into collision, and the detector components surround this point. Closest to the interaction point is the *tracking system*, which uses ionization to record the passage of charged particles. A magnetic field is present in the tracking system, and curves the particle trajectories. The direction of curvature with respect to the field reveals the charge of the particle, and the momentum can be determined from the curvature of the track trajectory. The tracking system can include a vertex detector, and measures the location of particle interactions.

Next are the electromagnetic and hadronic *calorimeters*, which measure the energy of an impinging particle by completely stopping it. Additionally, the pattern of the energy deposition by the particle reveals if it interacted electromagnetically or hadronically (i.e. via the strong interaction). This energy measurement is destructive, and only muons and neutrinos survive beyond the calorimeters.

Muons are much more massive than electrons, so they do not experience significant energy loss due to bremsstrahlung and do not get stopped by the calorimeters. Therefore they can be easily identified as tracks in the *muon system*, the outermost detector layer. Neutrinos, which do not interact via the strong or electromagnetic interaction, do not get detected by such particle detectors. However, the neutrino momentum and energy can be deduced from the imbalance in the momenta of the detected particles.

When quarks or gluons are produced in a collision, they hadronize due to color confinement and produce ensembles of hadrons called *jets*. The hadrons in these jets are detected, and quark flavor tagging methods are used to determine the type of quark that produced the jet. For the identification of heavy jets (from b or c quarks), *vertexing* is especially important. For instance, B mesons have a long enough lifetime (picosec-

onds) to fly a small distance before decaying. Therefore, they are identified through the presence of tracks propagating from a secondary vertex (SV) that is displaced from the primary vertex (PV) as shown in Figure 1.4. Similarly, τ leptons also fly a small distance before decaying, creating a secondary vertex. For flavor physics and accurate particle identification, it is important that a detector has good vertex resolution and accurate reconstruction of secondary vertices.

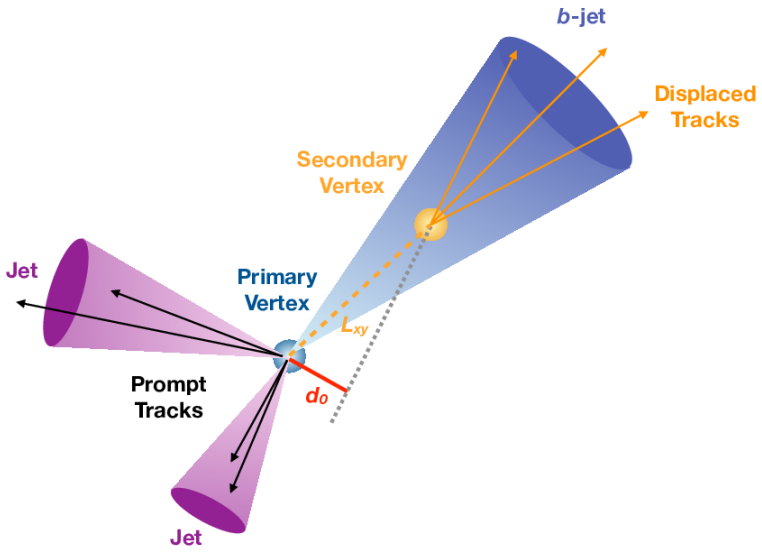

Figure 1.4: Schematic diagram of two light jets and one b-jet originating from a primary vertex. B-hadrons decay after a certain distance, resulting in a secondary vertex from which displaced tracks propagate [10].

1.3 Proposed Detector Concepts

The FCC-ee, as a circular collider, will have two to four interaction points, which allows for several complementary experiments to run concurrently. There are three detector designs currently being studied and optimized, namely the CLD detector, IDEA detector, and Noble Liquid calorimeter [2].

The *CLD detector concept* [11] is taken from CLIC and modified for FCC-ee purposes. It is comprised of a silicon tracker and vertex detector, a silicon-tungsten ECAL and a scintillator-steel HCAL (both with high granularity), a magnet, and resistive plate muon chambers interleaved within the steel return yoke.

The *IDEA detector concept* [12] has been designed specifically for circular e^+e^- colliders. The hallmark of the IDEA detector is its transparency to radiation. As illustrated in Figure 1.6, it is made of a silicon pixel vertex detector (VTX), a large-volume and extremely light wire drift chamber (DCH) surrounded by a silicon wrapper layer, a magnet, a pre-shower detector, a dual-readout calorimeter, and muon chambers within the magnet return yoke.

Both the CLD and IDEA detector concepts use a superconducting solenoid to generate a magnetic field of 2T. However, in the CLD detector it is a conventional solenoid surrounding the calorimeters, while in the IDEA detector it is a very thin ($< 1\,X_0$), light,

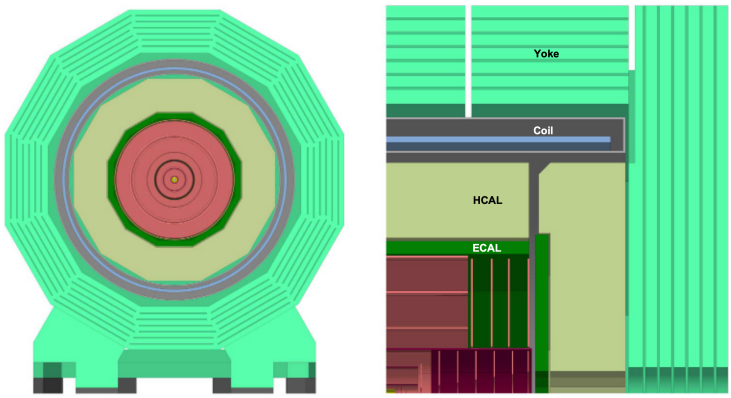

Figure 1.5: Schematic layout of the CLD detector. Transverse cross section (left) and longitudinal cross section of the top right quadrant (right) [2].

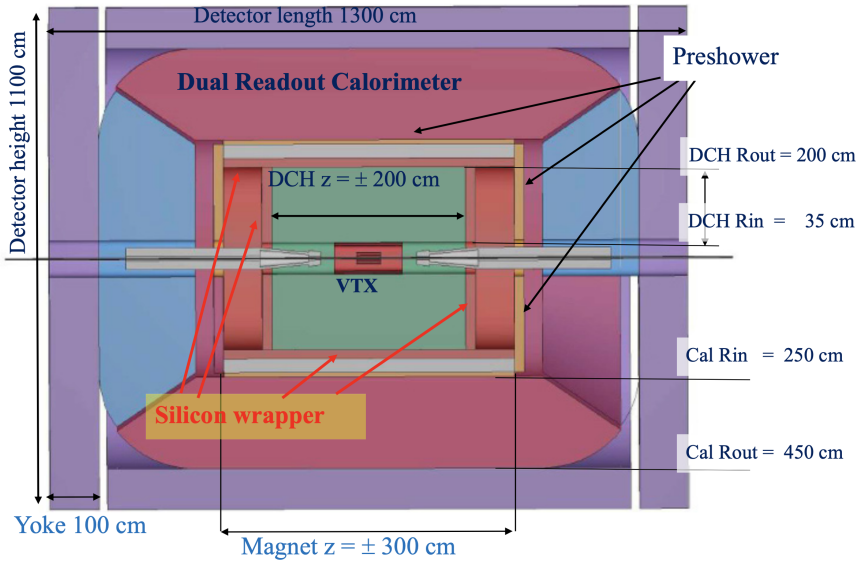

Figure 1.6: Schematic layout of the IDEA detector [2].

radiation-transparent solenoid positioned in front of the dual readout calorimeter. X_0 is the *radiation length*, which is the average distance after which a high energy electron has lost all but $\frac{1}{e}$ of its energy to bremsstrahlung [13]. The placement of the magnet is a balance between having it close enough to the detector's center to deliver a strong magnetic field, and not having the magnet material interfere with the particle trajectory and momentum before measurement.

The *Noble Liquid calorimeter* is a detector that strives to meet the need for high hadronic energy resolution at the FCC-ee. This type of calorimeter (also used in ATLAS at the LHC for example [14]) uses a liquified noble gas as the active material, and measures the ionization charge produced inside the liquid by a particle [15].

Both the CLD and IDEA detectors use similar vertex detector designs. The following Chapter 2 focuses on the vertex detector and track reconstruction, and discusses how it can be improved.

Chapter 2

Vertexing at FCC-ee

The reconstruction of the place of interaction (vertices) of particles is of great importance in high energy particle collisions. Section 1.2 discussed how the precise reconstruction of the vertices is of upmost importance for the identification of heavy jets and tau leptons. This Chapter introduces the vertex detector and important track parameters, and motivates the importance of material reduction in detectors.

2.1 Reconstruction of Vertices

Reconstructing the trajectory of a particle is done using multiple position measurements. At every detector layer, the charged particle ionizes the detector material. This ionization charge generates a signal in the sensor, which is read out, and a detector hit at that location is registered. Track reconstruction is generally divided into two tasks: track finding and track fitting. Track finding involves classifying detector hits into groups that might have been made by the same particle. Track fitting then takes these track candidates, decides if they indeed belong together, and calculates the 5 track parameters that uniquely describe a particle's track, as well as their uncertainties [16]. Two of these parameters that are important for describing tracks are the *transverse* and *longitudinal impact parameters*, D_0 and Z_0, which are illustrated in Figure 2.1. D_0 is the distance from the point of closest approach of a track to the beam line, and Z_0 is the z-coordinate of the point of closest approach.

2.2 Importance of Material Budget

When particles pass through matter, they encounter the electrons of the atom as well as the nucleus. Section 1.2 discussed that the energy imparted by a particle on the matter it is traversing can be used to detect it. Generally, the interactions that include a sizeable energy transfer are those with the atomic electrons. The atom's nucleus, on the other hand, is much more massive and therefore interactions with it do not change the particle's energy significantly. Rather, the main effect of the particle's interaction with the nucleus is a change in its trajectory. This scattering on a single nucleus is called coulomb scattering.

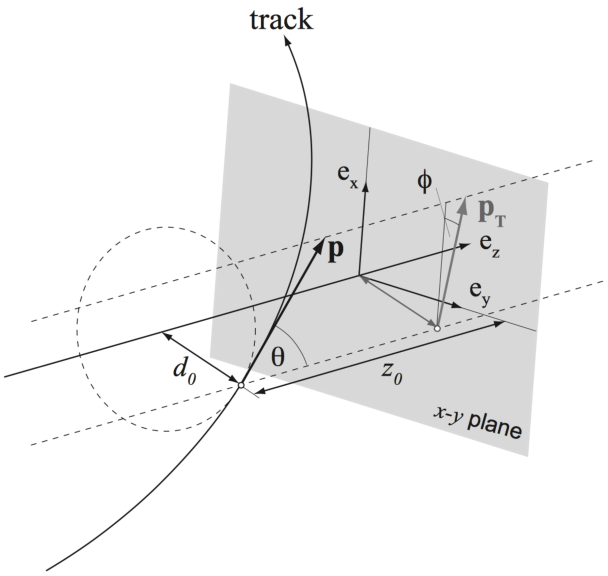

Figure 2.1: Illustration of the parameters that define a charged particle track [17].

If a particle traverses a material of a thickness x so that it scatters off many nuclei, each interaction results in a small random change in its trajectory. This process is called *multiple scattering*, and is illustrated in Figure 2.2. Here the net scattering distribution can be assumed to be gaussian with the central limit theorem. Strictly, the tails of this angular distribution are non-Gaussian (due to hard scattering that occurs less frequently, but occurs nevertheless). However the Gaussian approximation is used for the central 98% of the distribution. Defining $\theta_0 = \frac{\theta}{\sqrt{2}}$ to be the projection of the solid angle θ (that encloses 98% of the scattered beam) onto a plane, the angular deviation of the particle's trajectory can be calculated as

$$\theta_0 = \frac{13.6\text{MeV}}{\beta cp} z \sqrt{x/X_0} \left[1 + 0.038 \ln\left(x/X_0\right)\right]. \tag{2.1}$$

$\frac{x}{X_0}$ is the thickness of the material in radiation lengths, and p, βc, and z are the momentum, speed, and charge of the particle respectively [13]. Therefore, increasing $\frac{x}{X_0}$ leads to an increase in the angular deviation of the particle due to multiple scattering.

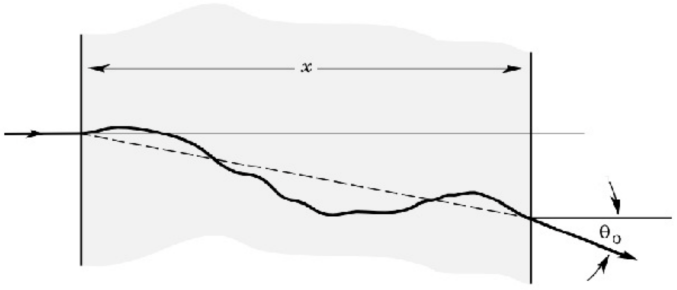

Figure 2.2: Illustration of multiple scattering resulting in a change in track trajectory [18].

The goal of the tracking system is to measure particle tracks to reconstruct trajectories. Clearly, the presence of detector layers is itself introducing changes in the trajectory to be measured, because of multiple scattering in the material. Therefore the impact parameter resolution depends not only on the intrinsic measurement uncertainty of the detector layers (the single-hit resolution), but also on the *material budget*, or how much material the particle that is measured has to traverse. Indeed, the expression for the transverse impact parameter resolution is often separated into two terms as written in Equation (2.2), where a represents the intrinsic uncertainty, and b represents the uncertainty from multiple scattering [19]:

$$\sigma_{D_0} = a \oplus b/p \sin^{3/2}\theta = (a^2 + b^2/(p^2 \sin^3\theta))^{1/2}. \tag{2.2}$$

Notice that the resolution depends on the momentum and the polar angle. Particles with higher momentum are influenced less by multiple scattering effects. An explanation of the derivation of fit function can be found in References [19] and [20].

2.3 Benefits of ALICE ITS3-like Vertex Detector Designs

Lower material budget detectors are clearly advantageous, as they disturb the particle less in the process of measuring it. What kinds of sensors are used and how can the material budget be reduced? Traditionally, tracking detectors utilize hybrid pixel sensors, where the read-out electronics are connected to the sensor using bump bonding as shown in Figure 2.3.

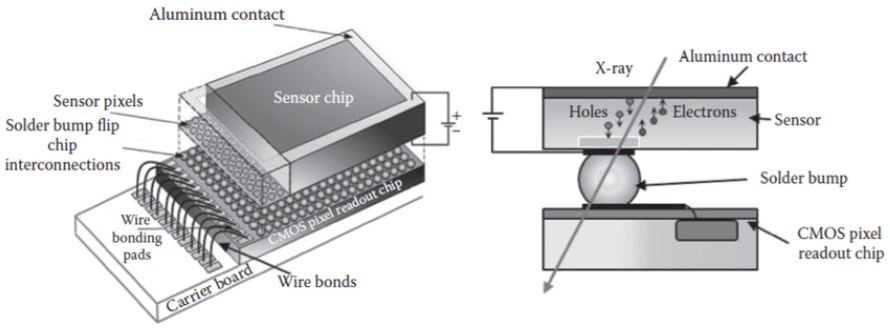

Figure 2.3: Example of a hybrid pixel detector [21].

Monolithic Active Pixel Sensors (MAPS), on the other hand, have the read-out electronics integrated in the sensor die, which makes the mass production of sensors simpler by eliminating the need for the expensive bump bonding procedure, and also allows for the complete sensor to be thinner [22]. DMAPS are depleted monolithic active pixel sensors. Depletion is required for fast charge collection. An impinging particle on the sensor will ionize the material and create electron-hole pairs in the depletion region, which drift apart in the electric field, yielding the electrical signal that indicates that a particle has passed through [23].

The ALICE (A Large Ion Collider Experiment) detector has the first MAPS-based Inner Tracking System (ITS) at the LHC, which was installed during Long Shutdown 2 (LS2) [24]. For LS3, which is scheduled for 2026, the collaboration plans another upgrade to

get closer to the interaction point and reduce the material budget further: the ALICE ITS3 project [25]. This upgrade will rely on the ability to produce wafer-scale DMAPS sensors, and on the flexibility of thin silicon. Thinner sensors (20-40 μm) can be bent to form curved sensors [26]. As illustrated in Figure 2.4a, large curved sensors not only reduce the material budget, but also lead to a more uniform distribution of material and a smaller average radius of the layer.

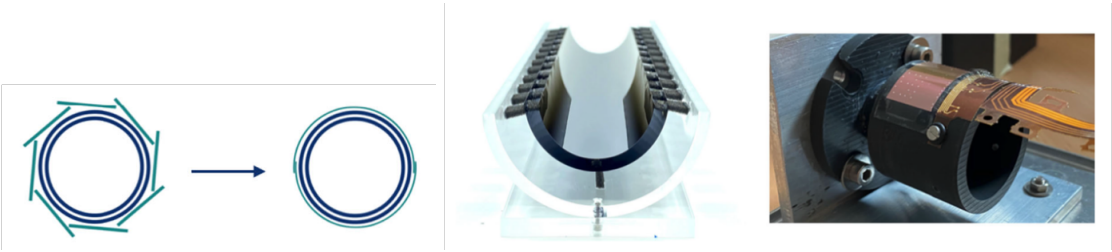

(a) (b)

Figure 2.4: (a) A schematic of how curved sensors can reduce the average radius of a detector later and (b) prototypes of curved silicon sensors [27].

Looking at the contribution of different parts of the detector to the material budget of the ALICE ITS2 in Figure 2.5, one can see that silicon constitutes only a small fraction of the total material budget, and that the amount of material is not uniformly distributed around the detector. The goal of the ITS3 project is to eliminate the additional contributions from all materials except for the silicon sensors themselves: water cooling can be removed given low power consumption enabling air cooling, circuit boards can be removed if the readout can be integrated on the chip, and mechanical supports can be removed thanks to the stiffness of the rolled silicon sensors.

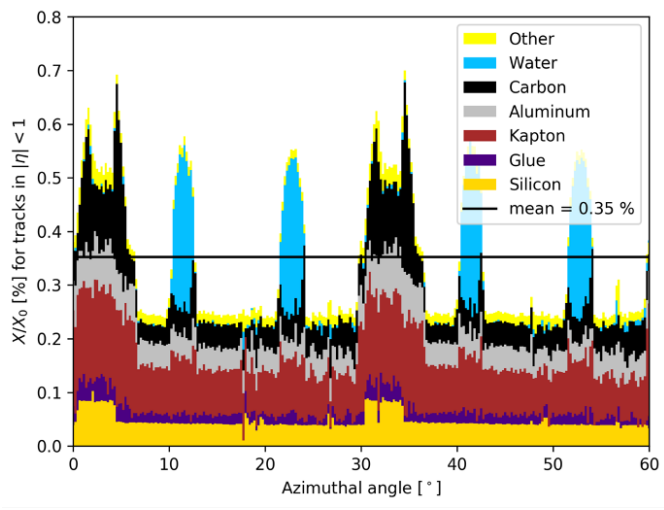

Figure 2.5: Material budget of the ALICE ITS II [28], showing the thickness of the materials in radiation lengths as a function of the azimuthal angle.

This thesis discusses the advantages of using similar curved sensor technology also in the vertex detector of the IDEA detector concept for FCC-ee, with the goal of improving impact parameter resolution and secondary vertex reconstruction, improving for example the flavor tagging performance.

Chapter 3

Simulation of the IDEA Detector

In order to study the impact of a low material budget vertex detector on particle track reconstruction, particle collisions and the response of different IDEA vertex detector geometries are simulated. This chapter describes these simulations, the different vertex performance metrics used, and the various IDEA vertex detector geometries studied. We use the FCC software framework, which is being developed using the Key4Hep software stack [29]. The Key4Hep project was started in 2020, and aims to provide a common set of tools (libraries for generation, simulation, reconstruction, and analysis of events) to be used by present-day and future high energy physics experiments. The Key4Hep release used in this work is key4hep-stack/2023-01-09.

3.1 Simulation of Particle Interactions using Monte Carlo Generators

To design, study, and optimize particle detectors and the reconstruction techniques of particles, it is important to be able to simulate the detector response to particle collisions. The simulation of particle collisions in high energy physics is done using Monte Carlo (MC) event generators. When two particles interact, it is not predetermined what the final state particles will be. MC generators use random numbers to model the interaction of particles with the same probabilities as in nature [30]. We use `Pythia8` [31], a general purpose MC event generator, and `EvtGen` [32], a MC event generator used to simulate the decays of B mesons. In general, simulating the physics of collisions in these generators is broken up into several parts. This includes the main hard scattering process, the ensuing radiation of particles, the secondary soft scattering processes, and the decay of certain particles inside the detector [33].

As for the detector simulation, generally GEANT full simulation [34] is used for accurate simulation of particle interactions with the detector materials. However, for quick phenomenological detector studies and to quickly compare many different detector layouts, a simpler parametric detector response simulation is sufficient. The DELPHES framework [35] allows for such fast parametric simulations. The simulation includes the main detector components, namely a tracking system inside a magnetic field, electromagnetic and hadronic calorimeters, and a muon system. All the elements are cylindrically sym-

metric around the beam axis. For the simulation of particle propagation in the tracker, DELPHES calculates the helicoidal (for charged particles) or straight (for neutral particles) track within the magnetic field that is parallel to the beam axis. They are then reconstructed as tracks with a certain probability. We use DELPHES for the IDEA detector in the simulation. The original detector geometry configuration that is currently in the FCC software framework is referred to as the `standard IDEA`[1] geometry. Modifications to the detector geometry will be discussed in Section 3.3.

As in most particle physics experiments, the IDEA detector uses a right-handed coordinate system with the origin at the nominal interaction point in the center of the experiment. The z-axis points along the beam axis, the x-axis points radially inwards to the center of the FCC ring, and the y-axis points vertically upwards. The polar angle θ is measured from the z-axis. The azimuthal angle ϕ is measured from the x-axis, sweeping out an angle in the x-y plane, which is referred to as the transverse plane. The transverse momentum p_{T} is the components of the momentum that lies within this plane transverse to the beam direction, and due to conservation of momentum it is a useful quantity. The transverse momentum is related to the total momentum $\mathbf{p}$ and the polar angle as follows:

$$p_{\mathrm{T}} = \frac{|\mathbf{p}|}{\cosh\left(-\ln\left(\tan\left(\frac{\theta}{2}\right)\right)\right)}\,. \tag{3.1}$$

3.2 Vertexing Performance Metrics

Different metrics are used to study the vertex detector performance. In the following, the impact parameter resolution is determined using both $Z \to \mu^+\mu^-$ events, as well as a particle gun that generates muons emitted in specific directions with specific momenta. Finally, strange B meson decays are used to estimate the study flight distance and secondary vertex resolutions.

3.2.1 $Z \to \mu^+\mu^-$ Events

`Pythia8` is used to generate $Z \to \mu^+\mu^-$ events. Specifically, 50,000 of these events with a collision energy $\sqrt{s} = 91.188\,\mathrm{GeV}$ were generated[2]. Other parameters including a beam energy spread of 0.0602 GeV were also set. The resulting muons have varying momenta, distributed with a mean of around 45 GeV. The decay of Z bosons to muons is chosen because muons propagate through the entire detector, leaving tracks all the way to the outermost muon chambers. This process is also one that would be relatively common in real e^+e^- collisions.

The MC simulated $Z \to \mu^+\mu^-$ events can then be used to estimate the impact parameter resolutions. These are extracted from the reconstructed particles using an existing analysis script[3]. The following discussion includes some intermediate results for the `standard`

[1] https://github.com/HEP-FCC/FCC-config/blob/e8a2087661fe0d58d45945382c0008b6ba86c519/FCCee/Delphes/card_IDEA.tcl

[2] https://github.com/HEP-FCC/FCC-config/blob/e8a2087661fe0d58d45945382c0008b6ba86c519/FCCee/Generator/Pythia8/p8_ee_Zmumu_ecm91.cmd

[3] https://github.com/HEP-FCC/FCCAnalyses/blob/6044eee8975fe8a1ea9cfa4122b19b0efd5ceea0/examples/FCCee/vertex/validation_tkParam.py

`IDEA` detector configuration. Different vertex detector geometries will be discussed in Section 3.3. Figures 3.1 and 3.2 show histograms of the transverse and longitudinal impact parameters, and their resolutions. Cuts were made on the data to exclude particles that are not muons, namely some photons and electrons that were generated in the $Z \to \mu^+\mu^-$ events from bremsstrahlung. The values of Z_0 have a much larger spread than D_0 (-1000 to $1000\,\mu$m vs. -15 to $15\,\mu$m). This is because the luminous region for electron positron bunch collisions has an elongated shape, illustrated in Figure 3.3. This is reflected in the simulation with greater vertex smearing in the z-direction (300 micrometers, compared to a few nanometers or micrometers in y and x). This means that the position at which the collision happens in a bunch is a wide distribution in z, leading to a larger range of Z_0 values. However, the uncertainty or resolution of the longitudinal impact parameter σ_{Z_0} is nevertheless small (standard deviation of $3.195\,\mu$m).

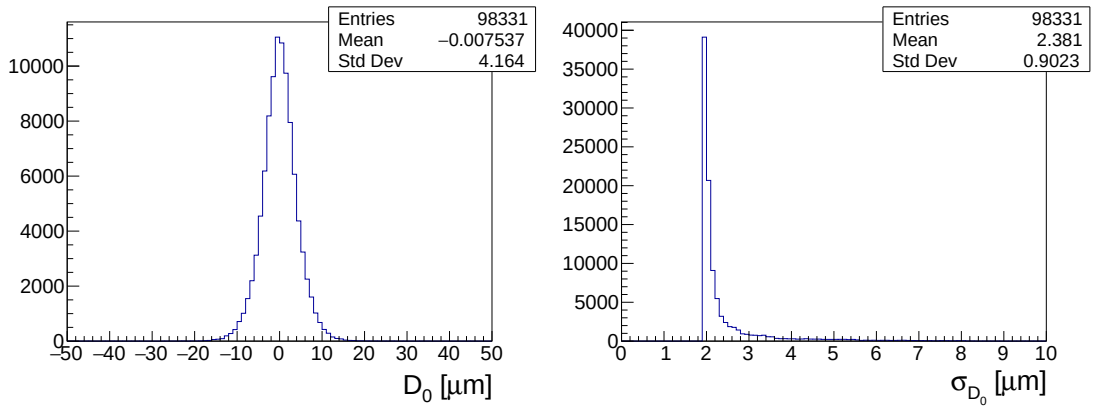

(a) (b)

Figure 3.1: Distributions of the transverse impact parameter and its resolution for $Z \to \mu^+\mu^-$ events in the `standard IDEA` detector configuration.

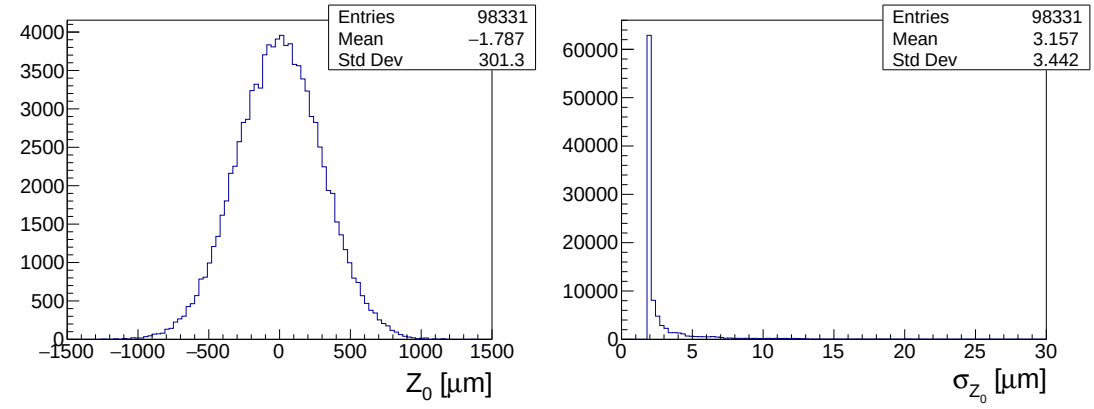

(a) (b)

Figure 3.2: Distributions of the longitudinal impact parameter and its resolution for $Z \to \mu^+\mu^-$ events in the `standard IDEA` detector configuration.

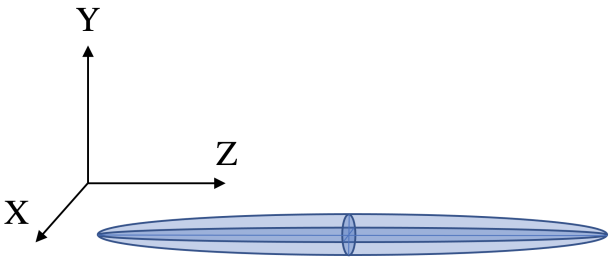

Vertex smearing:
sigmaVertexX $= 4.50 \times 10^{-3}$ mm
sigmaVertexY $= 20.0 \times 10^{-6}$ mm
sigmaVertexZ $= 0.03$ mm

Figure 3.3: Vertex smearing option used in DELPHES, and a schematic illustration of the luminous region of the e^+e^- collisions being most extended in the z-direction.

3.2.2 Particle Gun Muons

A particle gun can generate muons of specific momenta and flight direction. The benefit of using particle gun muons in addition to $Z \to \mu^+\mu^-$ events is that we will be able to study the impact of a lower material budget vertex detector on the track reconstruction of particles of high versus low momentum.

The tool used is a constant transverse momentum particle gun from k4SimDelphes[4]. To generate muons with defined total momentum, Equation (3.1) was used to calculate the transverse momentum p_T from the total momentum $\mathbf{p}$ and the polar angle. Using the particle gun, collections of 10,000 muons were generated, with momenta of 1, 10, and 100 GeV, flying out of the origin at polar angles of 10, 20, 30, 40, 50, 60, 70, 80, and 89 degrees.

Example distributions of the transverse impact parameter and its resolution are shown in Figure 3.4. The transverse impact parameter resolution is a very sharp peak with practically no variation. This is because the particle gun generates 10,000 near-identical muons that propagate in nearly exactly the same manner through the detector. This is in contrast to the wider histogram of the transverse impact parameter resolution of the $Z \to \mu^+\mu^-$ events in Figure 3.1.

3.2.3 Strange B Mesons

To study the impact of reducing the material budget on secondary vertex and flight distance resolution, `Pythia8` and `EvtGen` were used to generate 100,000 events where strange B mesons $\left(B_s^0 = s\bar{b}\right)$ are produced in e^+e^- collisions at $\sqrt{s} = 91.188\,\mathrm{GeV}$[5]. The B_s^0 mesons propagate a certain flight distance before decaying into a $J/\Psi\,(c\bar{c})$ and a $\Phi\,(s\bar{s})$ meson at the secondary vertex. These then decay very swiftly into $\mu^+\mu^-$ and $K^+\,(u\bar{s})\,K^-\,(s\bar{u})$ respectively. Thus, the four tracks of the muons and Kaons propagate out from the secondary vertex.

[4] https://github.com/key4hep/k4SimDelphes/blob/1e647bb9b4bc81a3bdf3f3bef5015bda95dabd8f/framework/k4SimDelphes/examples/options/k4simdelphesalg.py

[5] https://github.com/HEP-FCC/FCC-config/blob/e8a2087661fe0d58d45945382c0008b6ba86c519/FCCee/Generator/Pythia8/p8_ee_Zbb_ecm91_EVTGEN.cmd (Pythia8 configuration file)
https://github.com/HEP-FCC/FCC-config/blob/e8a2087661fe0d58d45945382c0008b6ba86c519/FCCee/Generator/EvtGen/Bs2JpsiPhi.dec (EvtGen configuration file)

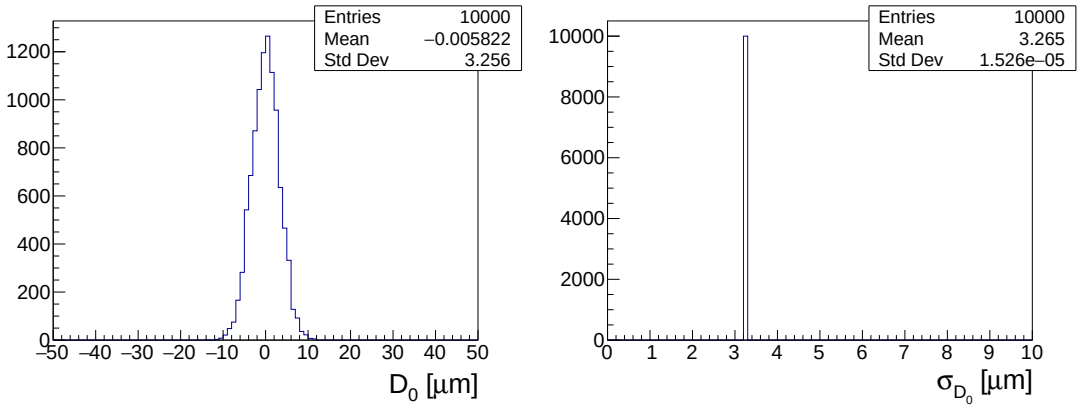

(a) (b)

Figure 3.4: Distributions of the transverse impact parameter and its resolution for particle gun muons generated with a momentum of 10 GeV at a polar angle of 70 degrees.

The two metrics to be studied are the *flight distance resolution* and *secondary vertex resolution*, which are illustrated in Figure 3.5. The flight distance resolution is the difference in flight path length measured from the primary vertex to the MC secondary vertex, versus to the reconstructed secondary vertex:

$$\text{flight distance resolution} = ||\vec{x}_{\text{MC SV}} - \vec{x}_{\text{PV}}| - |\vec{x}_{\text{Reco SV}} - \vec{x}_{\text{PV}}||. \tag{3.2}$$

The secondary vertex resolution is the distance from the reconstructed secondary vertex to the MC secondary vertex, which is calculated by taking the 3D position vector of these two points and subtracting them:

$$\text{secondary vertex resolution} = |\vec{x}_{\text{MC SV}} - \vec{x}_{\text{Reco SV}}|. \tag{3.3}$$

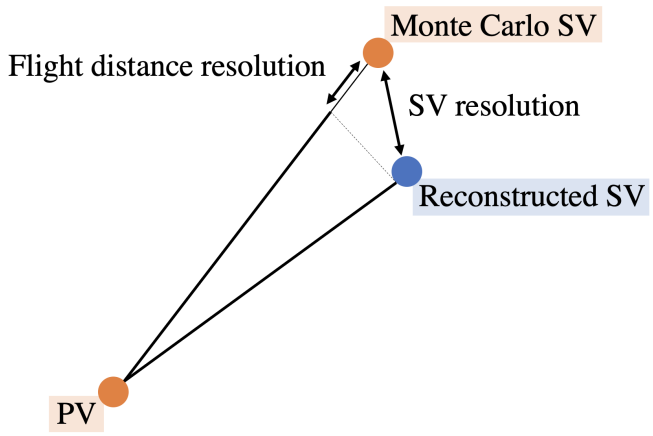

Figure 3.5: Illustration of flight distance resolution and secondary vertex resolution.

To reconstruct the secondary vertex, the LCFI+ software [36] is used. This has recently been implemented in the FCC software framework, and includes vertex finding algorithms for the identification of primary and secondary vertices [37].

The distribution of the secondary vertex resolutions includes several very large outliers, since if the selected MC vertex does not correspond to the reconstructed vertex, the distance between these points will be very high. An upper cut was placed at 500 μm, as well as a condition that the chi squared of the vertex fit is less than 10, and that the B_s^0 decay vertex has been found. A scatter plot of the secondary vertex resolution for the standard IDEA detector with these cuts applied is shown in Figure 3.6.

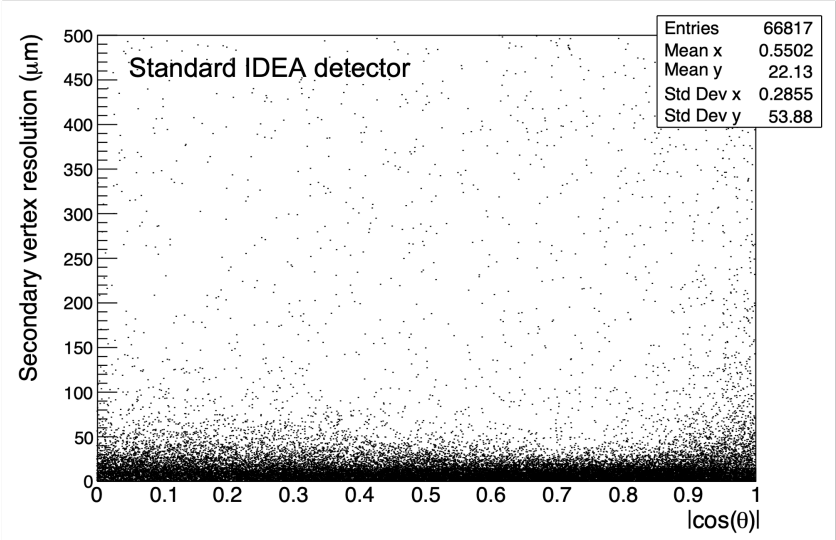

Figure 3.6: Scatter plot of secondary vertex resolution with cut at 500 μm.

3.3 Vertex Detector Geometry Configurations

As discussed in Section 2.3, the goal of this work is to estimate the performance of a modified IDEA vertex detector for a reduced material budget detector based on the curved DMAPS sensors explored in the ALICE ITS3. The IDEA vertex detector is cylindrically symmetric and centered around the beam pipe, as shown in Figure 3.7. The base version of the detector used in this study is composed of three cylindrical inner vertex layers, eight vertex disc layers, and two cylindrical outer vertex layers.

The starting point for the geometry modifications is the original detector geometry configuration card that is currently in the FCC software framework, which was introduced in Section 3.1 and is referred to as the `standard IDEA` geometry. There have been recent design changes to the beam pipe and innermost vertex detector layer that are not yet included in the configuration card that are described in References [38] and [39]. Namely, the beam pipe radius has been reduced, and the first vertex layer has been moved closer to the beam pipe. These changes are implemented in a modified detector configuration card referred to as `+R1.3` in Table 3.1.

The next step is to change the material budget of the vertex detector, which is done by changing the width (i.e. thickness) of the vertex layers. The original thickness of each layer was 280 μm, which is about the thickness of not thinned DMAPS used in high energy physics. For curved silicon sensors as discussed in Section 2.3, the thickness is 20 to 40 μm (thicker sensors are not flexible enough to be bent). The different vertex detector geometry configurations used are listed in Table 3.1. The thickness of the

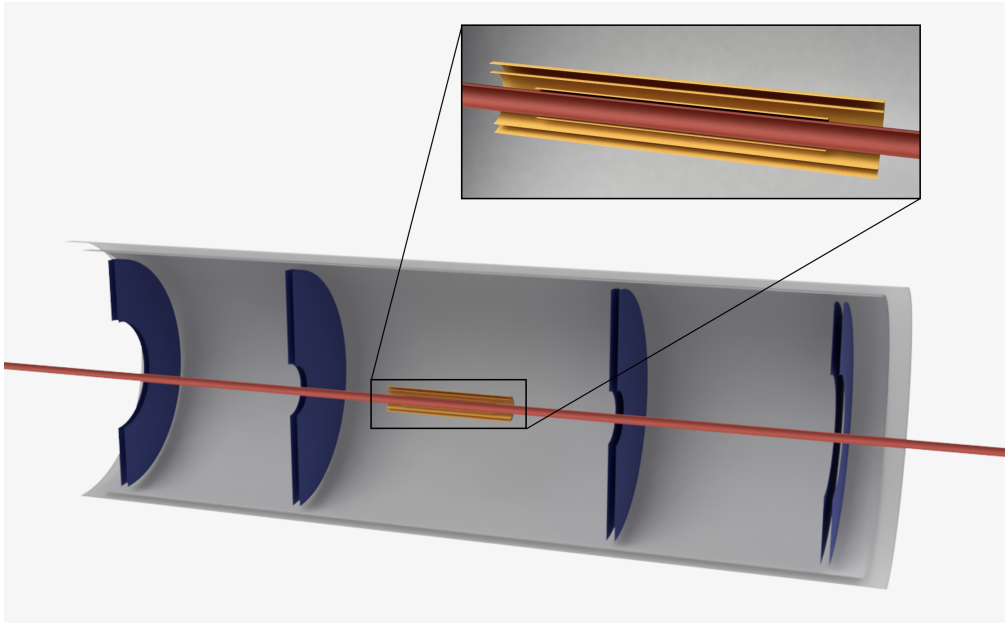

Figure 3.7: Schematic cross section view of the original IDEA vertex detector, including the beam pipe (red), three inner VTX layers (yellow), eight VTX disc layers (blue), and two outer VTX layers (gray).

first three vertex layers is reduced to 30 μm for the ideal material budget of curved silicon sensors (`+w30`), and two configurations with more conservative thicknesses of 50 and 100 μm are also included to account for some extra material contributions (`+w50` and `+w100`). Additionally, the thickness of the eight vertex disc layers is reduced in addition to the first three vertex layers (`+w30_DSK`, `+w50_DSK` and `+w100_DSK`). Lastly, in the configuration `+L1_w30` only the thickness of the first barrel vertex layer is reduced to 30 μm. The motivation behind this is that this first layer can be constructed with one single wafer-sized sensor, while the following layers become too large and must be constructed by combining multiple silicon wafers.

Name	Beam pipe radius [cm]	VTX layer$_1$ radius [cm]	Thickness of first 3 VTX layers [μm]	Thickness of 8 VTX disc layers [μm]
standard IDEA	1.5	1.7	280	280
+R1.3	1	1.3	280	280
+w100	1	1.3	100	280
+w50	1	1.3	50	280
+w30	1	1.3	30	280
+w100_DSK	1	1.3	100	100
+w50_DSK	1	1.3	50	50
+w30_DSK	1	1.3	30	30
+L1_w30	1	1.3	layer$_1$ = 30, layer$_{2,3}$ = 280	280

Table 3.1: Different vertex detector geometries.

The following Chaper 4 will discuss the results of the three vertex detector performance metrics for these different geometries.

Chapter 4

Results and Discussion

This chapter presents the results from the three vertexing performance metrics and compares them for the different material budget IDEA vertex detector geometries.

4.1 Impact Parameter Resolution

From simulations of $Z \to \mu^+\mu^-$ events, comparisons of impact parameter resolution for different vertex detector geometries can be made. Figure 4.1 shows the transverse and longitudinal impact parameter resolutions as a function of the polar angle for different vertex detector geometries. In the forward direction (small θ) the impact parameter resolution becomes worse. This dependence on the polar angle is described in Equation (2.2). In the $\theta \to 0$ limit where particles are emitted very much in the forward direction, nearly parallel to the beam pipe, they would not be measured at all. The detector coverage is down to about 8.7 degrees.

Figure 4.1 shows the transverse and longitudinal impact parameter resolutions, comparing the `standard IDEA`, `+R1.3`, and the lower material budget geometries `+L1_w30`, `+w100`, `+w30`, and `+w30_DSK`. The impact parameter resolution is already improved with the smaller beam pipe and closer innermost vertex layer (black to red points). Reducing the material budget by reducing the thicknesses of the three innermost vertex detector layers, first from 280 μm to 100 μm (red to green), then from 100 μm to 30 μm (green to blue) further improves the resolution. Even only minimizing the thickness of the first barrel layer already results in a significant improvement (red squares to pink circles).

In addition to reducing the material budget of the three innermost vertex detector layers, these changes may also be applied to the eight vertex disc layers. Figure 4.2 evaluates the added benefit of reducing the thickness of the disc layers by comparing the transverse and longitudinal impact parameter resolutions for thicknesses of 100 μm, 50 μm, and 30 μm with and without including disc layers. Reducing the material budget of the vertex disc layers in addition to the innermost barrel layers is a small improvement, which is especially visible in the forward direction. This is expected since particles emitted radially from the interaction point do not traverse the vertex disc layers (see Figure 3.7).

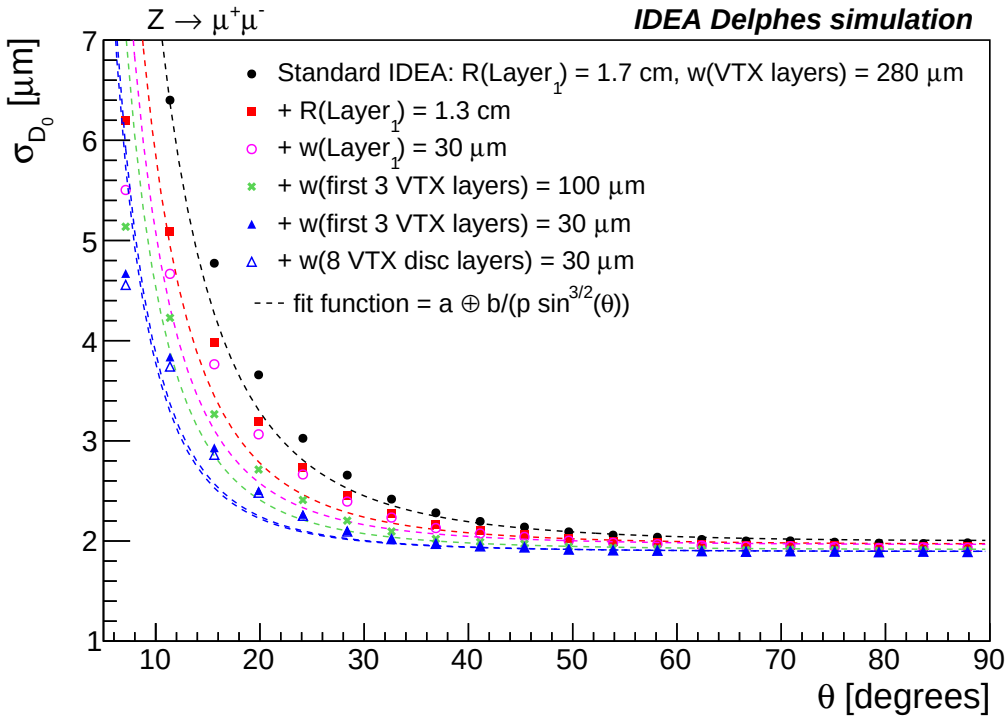

(a)

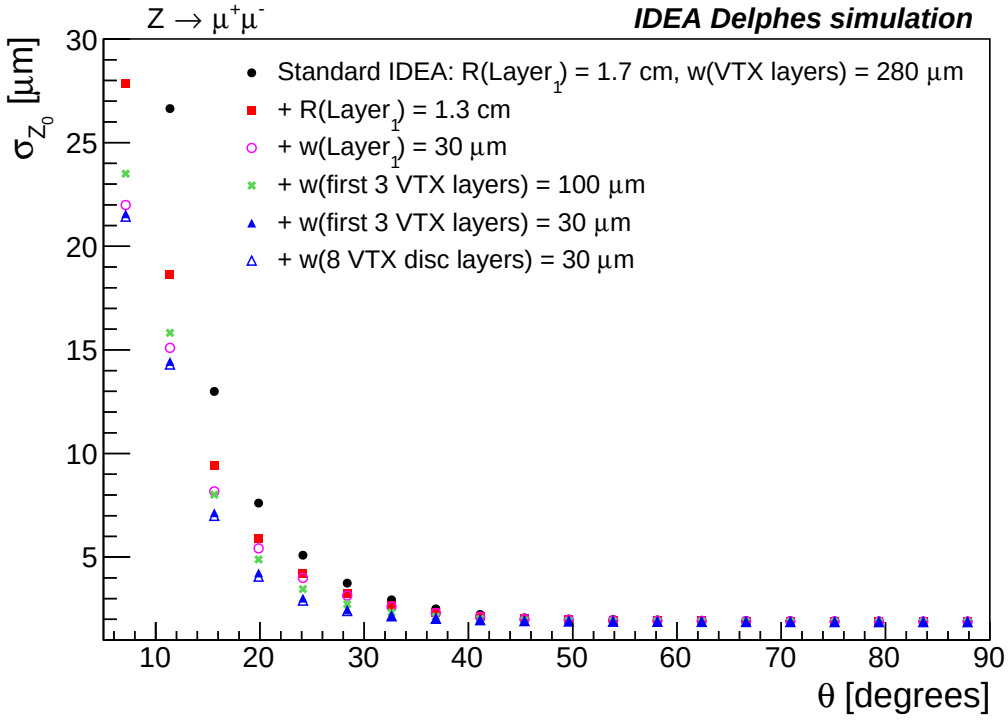

(b)

Figure 4.1: Transverse (a) and longitudinal (b) impact parameter resolution as a function of θ for different vertex detector geometry configurations.

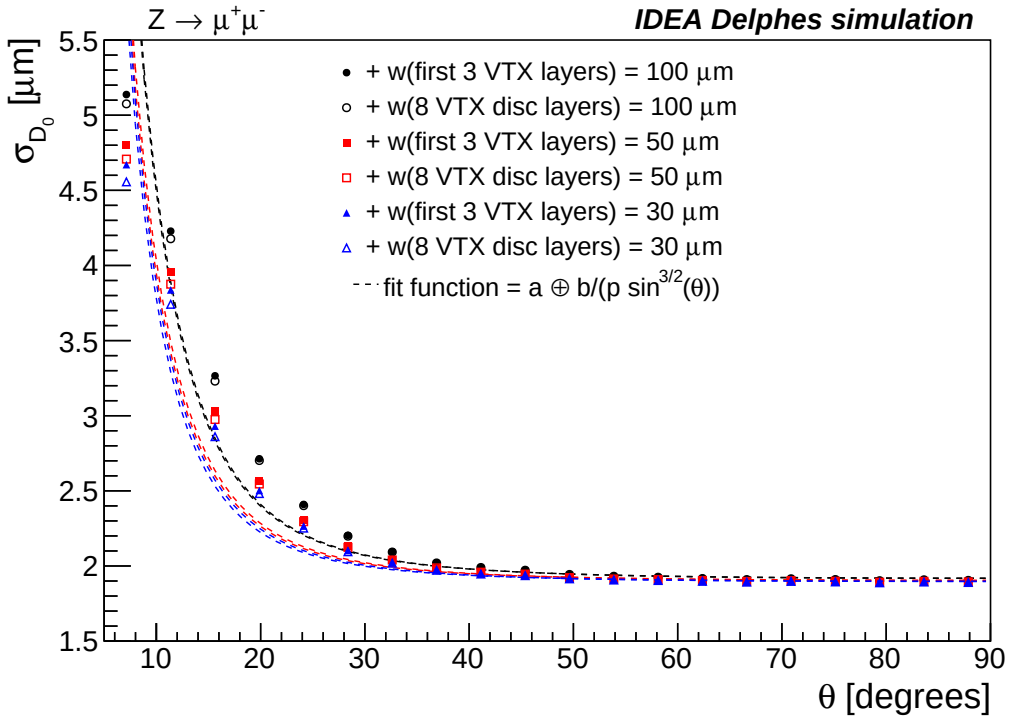

(a)

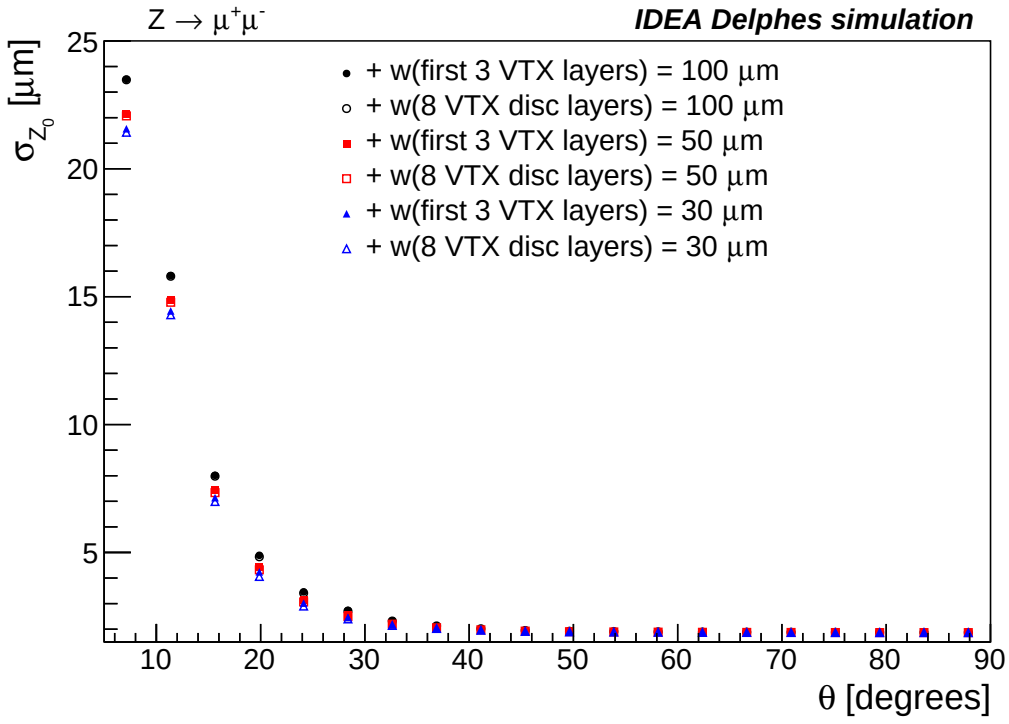

(b)

Figure 4.2: Transverse (a) and longitudinal (b) impact parameter resolution as a function of θ for different detector geometry configurations, looking at the effect of also reducing material budget in the VTX disc layers.

The data points for each geometry in Figures 4.1a and 4.2a are fitted with Equation (2.2), which factorizes the transverse impact parameter resolution, in order to extract the parameters a and b. The average momentum of the muons from $Z \to \mu^+\mu^-$ events is $44.44 \pm 4.209\,\text{GeV}$, and the momentum parameter was set accordingly for the fit. The values of a and b are listed in Table 4.1, and represent the contributions from the intrinsic detector uncertainty and from multiple scattering respectively. The fit parameter a remains constant with a value of about $1.9\,\mu\text{m}$ between the different geometries, while b decreases from around 16 to $11\,\mu\text{m} \cdot \text{GeV}$ (an improvement of about 30%) when the thickness of the three innermost vertex detector layers is reduced from $280\,\mu\text{m}$ to $30\,\mu\text{m}$. This is expected since when considering vertex detectors with lower material budget, nothing changes with the intrinsic uncertainty of the detector layers, but multiple scattering effects are reduced. Parameter b indeed decreases between each successive geometry.

Geometry	Parameter a [μm]	Parameter b [$\mu\text{m} \cdot \text{GeV}$]
Standard IDEA	1.9346 ± 0.0020	21.40 ± 0.06
+R1.3	1.9326 ± 0.0015	16.33 ± 0.92
+L1_w30	1.9375 ± 0.0012	14.36 ± 0.65
+w100	1.8948 ± 0.0011	13.03 ± 0.64
+w100_DSK	1.8959 ± 0.0010	12.91 ± 0.65
+w50	1.8863 ± 0.0009	11.78 ± 0.68
+w50_DSK	1.8873 ± 0.0009	11.60 ± 0.71
+w30	1.8811 ± 0.0008	11.44 ± 0.68
+w30_DSK	1.8829 ± 0.0008	11.19 ± 0.69

Table 4.1: Parameters extracted from the fit of Equation (2.2) on the transverse impact parameter resolution from $Z \to \mu^+\mu^-$ events in Figures 4.1a and 4.2a.

Insight into the momentum dependence of the impact parameter resolution is gained in Figure 4.3, where the particle gun introduced in Section 3.2.2 is used to create muons with fixed momenta. Comparing the three different momenta, 1 GeV (black), 10 GeV (red), and 100 GeV (blue), it is clear that low momentum muons have worse impact parameter resolution. When these low energy muons traverse the detector material, a larger fraction of the total momentum is lost. Thus, the impact parameter resolution is worse compared to high energy muons, which lose a smaller fraction of their total momentum. This momentum dependence is described in Equation (2.2). Furthermore, reducing the material budget has a greater effect on the low momentum muons than the high momentum ones (greater improvement from the black squares to black triangles than from the blue squares to blue triangles). This is because lower momentum particles are more effected by multiple scattering (see Equation (2.1)), the amount of which relates to the material budget. For all the momenta, the relative improvement using three layers with $30\,\mu\text{m}$ thickness is about as much as using the smaller beam pipe (the distance from circle to square and square to triangle in the log plot is similar).

As before, Equation (2.2) is used to fit the transverse impact parameter resolution in Figure 4.3a. The fit parameters a and b are given in Table 4.2. It should be noted that the fit did not converge for the momentum of 1 GeV, and that the errors of the fit parameters are too small to be trusted. However, for momenta of 10 and 100 GeV the parameter a consistently has a value around $1.9\,\mu\text{m}$, and parameter b indeed decreases with each successive vertex detector geometry (from `standard IDEA` to `+R1.3` to `+w30`).

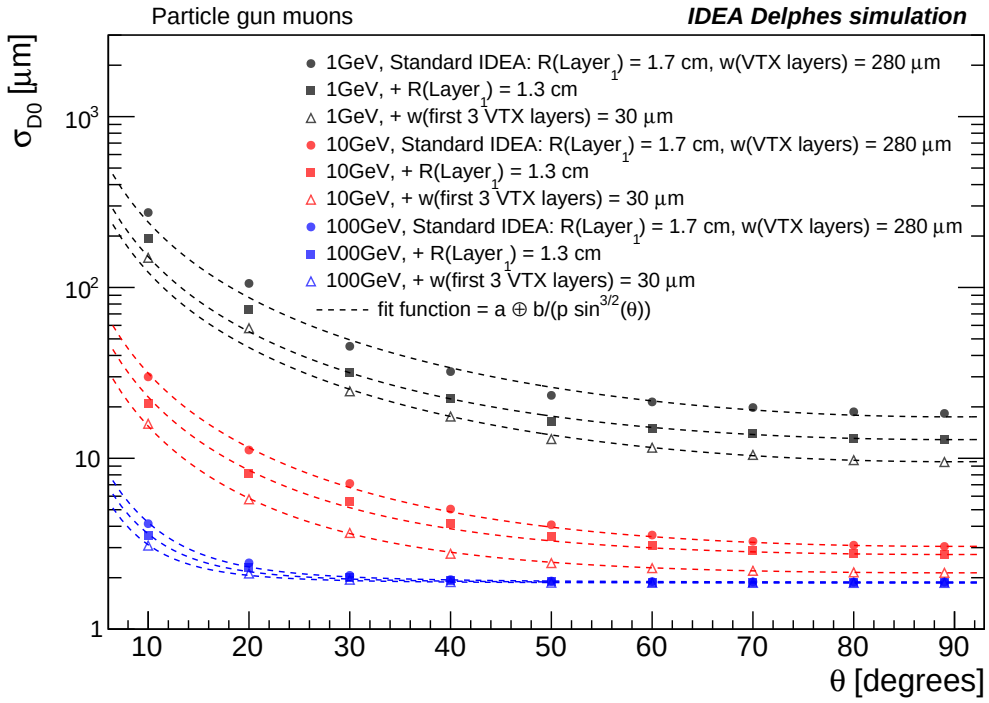

(a)

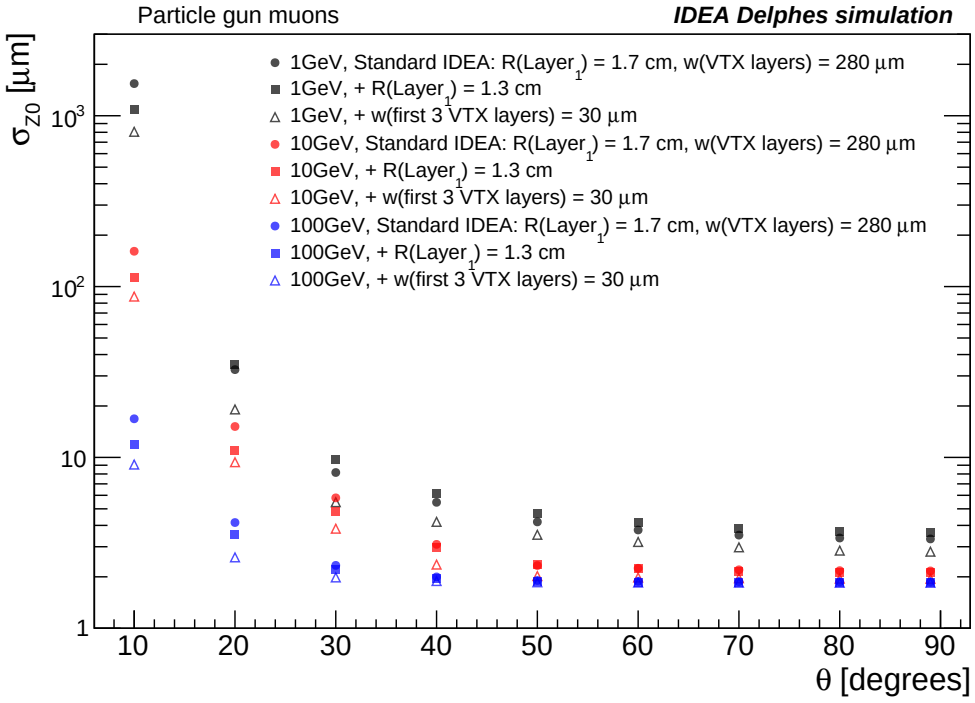

(b)

Figure 4.3: Transverse (a) and longitudinal (b) impact parameter resolution as a function of polar angle for different momenta (colors) and different vertex detector configurations (marker shapes).

Geometry	Momentum [GeV]	Parameter a [μm]	Parameter b [μm $\cdot$ GeV]
Standard IDEA	1	1.00000*	17.4524 $\pm$ 0.000002
+R1.3	1	6.76067 $\pm$ 0.0000105	10.9413 $\pm$ 0.000006
+w30	1	3.51491 $\pm$ 0.0000178	8.87756 $\pm$ 0.000006
Standard IDEA	10	1.81603 $\pm$ 0.0000317	24.4841 $\pm$ 0.000228
+R1.3	10	2.18280 $\pm$ 0.0000083	16.4586 $\pm$ 0.000103
+w30	10	1.82604 $\pm$ 0.0000045	11.0777 $\pm$ 0.000072
Standard IDEA	100	1.86872 $\pm$ 0.0000007	27.2306 $\pm$ 0.000199
+R1.3	100	1.85984 $\pm$ 0.0000005	22.3703 $\pm$ 0.000156
+w30	100	1.85420 $\pm$ 0.0000003	18.1184 $\pm$ 0.000231

Table 4.2: Parameters extracted from the fit of Equation (2.2) on the transverse impact parameter resolution in Figure 4.3a. *This fit parameter did not properly converge, and always takes the value of the lower parameter limit.

4.2 Flight Distance Resolution

For the flight distance resolution, Figure 4.5 shows four scenarios that use different combinations of reconstructed PV and SV, and are increasingly realistic. The scenarios are summarized in Table 4.3, and the choices of PV and SV are illustrated in Figure 4.4.

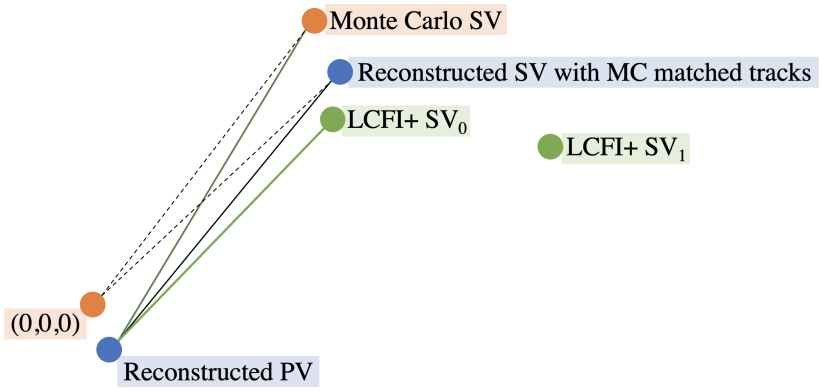

Figure 4.4: Schematic of the different choices of primary and secondary vertices used for calculating the flight distance resolution.

Case 1 is the most simple case considered, where the PV is the origin and the SV is reconstructed using the correct (MC matched) tracks. The fact that the correct four tracks belonging to the SV can be identified, is of course a big assumption. Case 2 is slightly more realistic, as it uses the reconstructed PV. Figure 4.5a compares cases 1 and 2 for the standard IDEA detector configuration. Using the reconstructed PV results in slightly worse flight distance resolution, which is expected since there is now an additional uncertainty contribution from the reconstruction of the PV. The flight distance calculated in this manner is compared for different detector geometries in Figure 4.5b. Realistically however, the information about which tracks belong to a given secondary vertex is not known. This motivates the next scenario, case 3, which no longer uses MC matched tracks, and instead considers the reconstructed secondary vertex to be all

possible reconstructed LCFI+ secondary vertices. The flight distance resolution using this definition is shown in Figure 4.5c, and is worse than when MC information was used, as expected. Finally for case 4, which we hypothesize will yield the most realistic flight distance resolution, only the LCFI+ secondary vertex that is closest to the MC SV is used. This assumption improves the resolution by roughly 10 μm from the previous case. Despite using MC information, the resulting resolution is most realistic since for SV reconstruction in fast simulation only tracks are used, and no other information such as particle identification. For example, if particle identification information were available, reconstruction of the B_s^0 secondary vertex could require two muon and two kaon tracks, improving the resolution on flight distance.

Case	Primary Vertex	Reconstructed Secondary Vertex
1	Origin	Reconstructed with MC matched tracks
2	Reconstructed	Reconstructed with MC matched tracks
3	Reconstructed	All reconstructed LCFI+ SV
4	Reconstructed	Closest reconstructed LCFI+ SV to MC SV

Table 4.3: Flight distance scenarios.

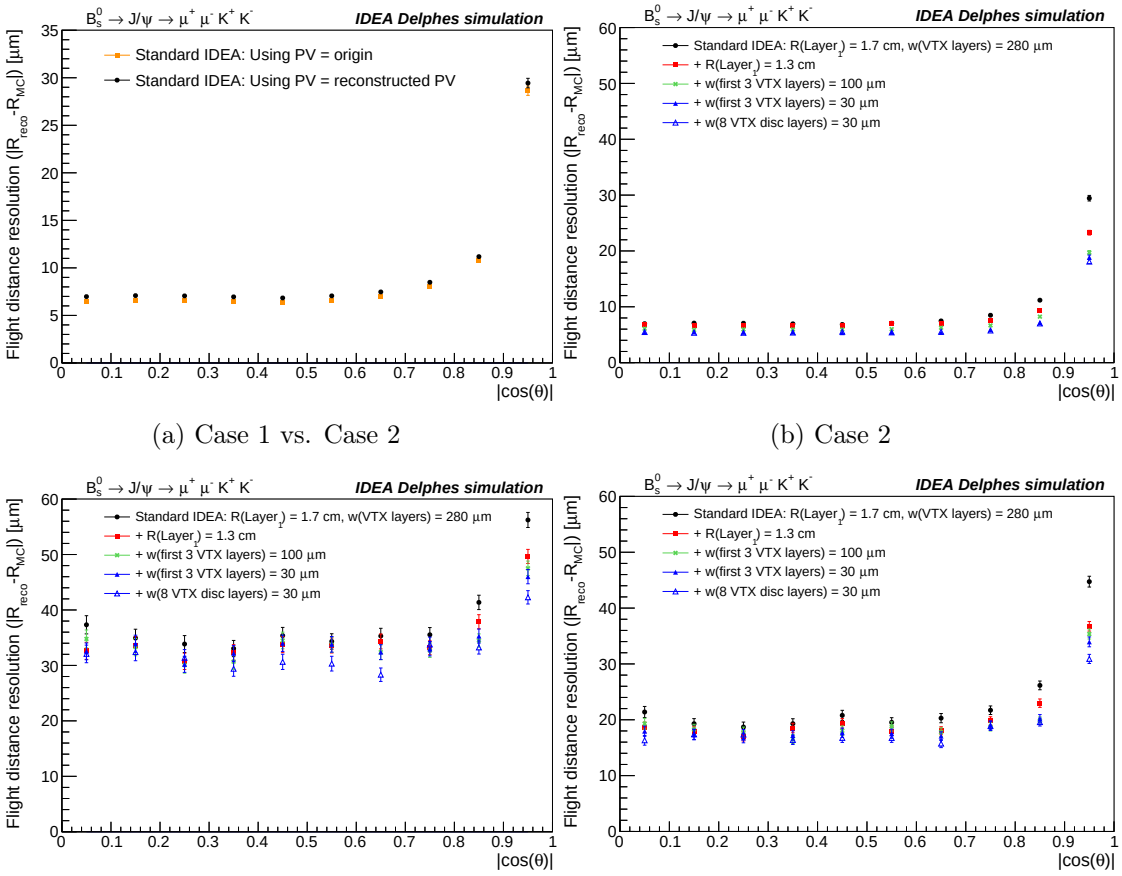

(a) Case 1 vs. Case 2

(b) Case 2

(c) Case 3

(d) Case 4

Figure 4.5: Flight distance resolution as a function of $|\cos(\theta)|$, where the cases (see Table 4.3) shown in successive plots are increasingly realistic.

One possible way to quantify the improvement in the flight distance resolution is to calculate the relative change between different geometries. This was determined for the scenario using the LCFI+ SV closest to the MC SV (Figure 4.5d). First, the relative change was calculated between each corresponding data point as follows:

$$\text{relative change} = \frac{\text{final} - \text{initial}}{|\text{initial}|}. \tag{4.1}$$

Then, the mean of these values was taken to obtain the average relative change of the flight distance resolution between the initial and final geometry. These values are listed in Table 4.4.

The error propagation calculation for relative change is as follows:

$$\Delta_{\text{change}} = \sqrt{\left(\frac{\partial \text{change}}{\partial \text{initial}}\right)^2 \cdot \Delta^2_{\text{initial}} + \left(\frac{\partial \text{change}}{\partial \text{final}}\right)^2 \cdot \Delta^2_{\text{final}}}, \tag{4.2}$$

where the partial derivatives are

$$\frac{\partial \text{change}}{\partial \text{initial}} = \frac{\partial}{\partial \text{initial}} \left(\frac{\text{final} - \text{initial}}{|\text{initial}|}\right) = \frac{-\text{final}}{\text{initial}|\text{initial}|} \tag{4.3}$$

and

$$\frac{\partial \text{change}}{\partial \text{final}} = \frac{1}{|\text{initial}|}. \tag{4.4}$$

Initial geometry	Final geometry	Percent change in FD reso [%]
Standard IDEA	+R1.3	-9.79 ± 1.69
+R1.3	+w100	-2.69 ± 1.90
+R1.3	+w30	-5.64 ± 1.86
+R1.3	+w30_DSK	-9.31 ± 1.81

Table 4.4: Average percent change of flight distance resolution between different combinations of initial and final geometry.

From this analysis, it is determined that reducing the radius of the beam pipe and moving the first barrel layer closer to to beam pipe (`standard IDEA` to `+R1.3`) results in an average change in flight distance resolution of $-9.79 \pm 1.69\%$. This means that it was improved by $9.79 \pm 1.69\%$. When the thickness of the innermost three vertex detector layers is reduced from 280 to 30 μm (`+R1.3` to `+w30`), the flight distance resolution is improved by around 5%.

4.3 Secondary Vertex Resolution

The secondary vertex resolution, introduced in Section 3.2.3, is shown in Figure 4.6 for different vertex detector geometries. Again, the average relative change between the geometries is chosen as a way to quantify the improvement in secondary vertex resolution. These values are listed in Table 4.5. Reducing the thickness of the innermost

three vertex detector layers to 30 μm (`+R1.3` to `+w30`) yields a $20.70 \pm 1.13\%$ improvement in SV resolution. Notably, only reducing the thickness of the first vertex layer (`+R1.3` to `+L1_w30`) already yields an improvement of $6.63 \pm 1.29\%$, while additionally reducing the thickness of the eight vertex disc layers (`+R1.3` to `+w30_DSK`) does not show significant improvement ($19.60 \pm 1.20\%$ compared to $20.70 \pm 1.13\%$ when the disc layers are left unchanged).

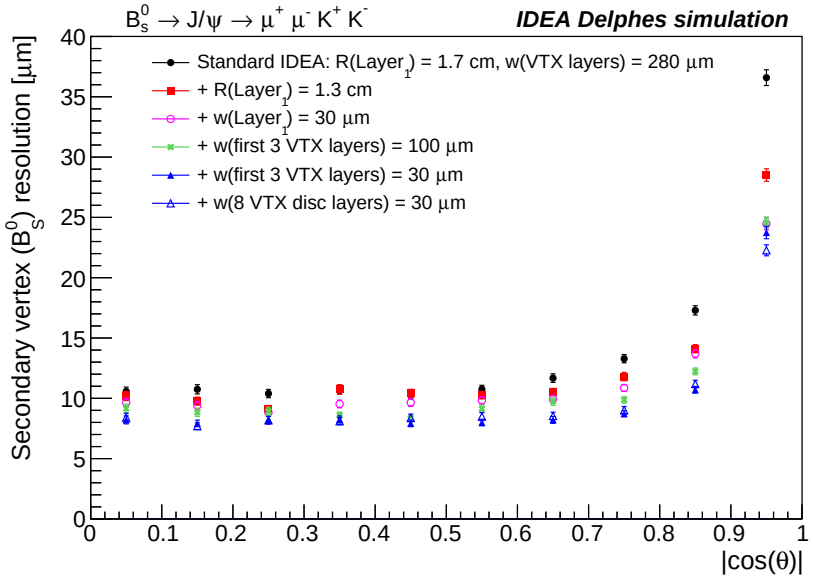

Figure 4.6: Secondary vertex resolution as a function of $|\cos(\theta)|$.

Initial geometry	Final geometry	Percent change in SV reso [%]	Error [%]
Standard IDEA	+R1.3	-8.91	1.25
+R1.3	+L1_w30	-6.63	1.29
+R1.3	+w100	-12.36	1.24
+R1.3	+w30	-20.70	1.13
+R1.3	+w30_DSK	-19.60	1.20

Table 4.5: Average percent change of flight distance resolution between different combinations of initial and final geometry.

Additionally, Table 4.6 lists the average relative change calculated separately for bins 1-5 (which correspond to $\cos(\theta) < 0.5$) and bins 5-10 (which correspond to $\cos(\theta) > 0.5$). This allows for a comparison of the improvement in the SV resolution in the forward versus radial direction. When the smaller beam pipe is adopted (`standard IDEA` to `+R1.3`), the improvement in SV resolution is very much concentrated in the forward direction. The SV resolution only improves by $4.62 \pm 2.03\%$ in bins 1-5, compared to an improvement of $13.20 \pm 1.46\%$ in bins 5-10. This makes sense, since the smaller beam pipe allows for the innermost vertex layer to be moved closer to the origin, which increases its angular coverage from 54.78 degrees to 47.29 degrees. Overall, the improvements are consistent with the improvements averaged over all the bins in Table 4.5.

Initial geometry	Final geometry	Percent change in SV reso in bins 1-5 [%]	Percent change in SV reso in bins 5-10 [%]
Standard IDEA	+R1.3	-4.62 ± 2.03	-13.20 ± 1.46
+R1.3	+L1_w30	-6.26 ± 2.03	-7.01 ± 1.59
+R1.3	+w100	-12.33 ± 1.96	-12.39 ± 1.53
+R1.3	+w30	-19.19 ± 1.80	-22.21 ± 1.36
+R1.3	+w30_DSK	-18.69 ± 1.88	-20.51 ± 1.48

Table 4.6: Percent change of flight distance resolution between different combinations of initial and final geometry, averaging separately over the first 5 bins ($\cos(\theta) < 0.5$) and last 5 bins ($\cos(\theta) > 0.5$) of the data.

Conclusions

The FCC-ee is a promising candidate for the next generation of particle physics experiments, yielding high precision measurements of the properties of the Standard Model particles that can reveal small deviations from the Standard Model. Vertexing is important for the identification of heavy jets, and particles such as the τ lepton that propagate a small distance from the primary vertex before decaying at a secondary vertex. The vertex detector needs to be able to accurately reconstruct these vertices. It should also be as lightweight as possible in order to minimize the amount of multiple scattering that particles experience on the detector material. This thesis set out to investigate the benefits of a reduced material budget IDEA vertex detector for the FCC-ee, based on the curved sensor technology developed for ALICE ITS3. DELPHES was used to perform fast simulation of detector response to $Z \to \mu^+\mu^-$ events, particle gun muons, and strange B Meson decays, in order to study impact parameter resolution, flight distance resolution, and secondary vertex resolution.

It was shown that reducing the material budget of the innermost vertex detector layers will improve detector performance. Fitting the transverse impact parameter resolution with $\sigma_{D_0} = a \oplus b/p \sin^{3/2}\theta$, it was found that the fit parameter a, related to the intrinsic detector uncertainty, remains constant at approximately $1.9\,\mu$m, while b, related to multiple scattering, decreases from around 16 to $11\,\mu\text{m} \cdot \text{GeV}$ when the thickness of the three innermost vertex detector layers is reduced from $280\,\mu$m to $30\,\mu$m. This is expected since when considering vertex detector geometries with lower material budget, nothing changes with the intrinsic uncertainty of the detector layers, but multiple scattering effects are reduced. Additionally, we find an improvement of about 6 percent in flight distance resolution, and an improvement of about 20 percent in secondary vertex resolution with this reduction of the thickness of the first three layers.

Even reducing only the thickness of the innermost barrel layer, which is the most easily achievable reduction due to the possibility of constructing it with one single silicon wafer, shows some improvement. For instance, the secondary vertex resolution is already improved by 6.6 ± 1.3 percent when just the thickness of the first barrel layer is reduced from $280\,\mu$m to $30\,\mu$m (compared to an improvement of 20.7 ± 1.1 percent when the thicknesses of all three innermost vertex layers are reduced).

Reducing the thickness of the first three vertex detector layers to only $100\,\mu$m serves as a more conservative estimate of the material budget than reducing the thickness to $30\,\mu$m. It was shown that even this results in a sizeable improvement. Fits on the transverse impact parameter resolution yield a reduction of parameter b from about 16 to $13\,\mu\text{m} \cdot \text{GeV}$ for a thickness of $100\,\mu$m (compared to a reduction to $11\,\mu\text{m} \cdot \text{GeV}$ for a thickness of $30\,\mu$m).

It is also concluded that reducing the material budget of the eight vertex disc layers yields a small additional improvement in vertex detector performance. There is some improvement in impact parameter resolution in the forward region, and in flight distance resolution. However the secondary vertex resolution shows no improvement within the error margins when the thickness of the vertex disc layers are reduced in addition to the three innermost barrel layers.

There are many possibilities for future studies that expand on this work, including how the reduction in material budget changes flavor tagging efficiency. One could also implement the use of precise time-of-flight measurements from timing layers in the detector to help with particle identification. Additionally, one could improve the estimation of the flight distance resolution by using particle identification information of the tracks, as this more accurately reflects how experimental data is analyzed.

Bibliography

[1] W. Barletta, et al., *Planning the Future of U.S. Particle Physics (Snowmass 2013): Chapter 6: Accelerator Capabilities*, https://arxiv.org/abs/1401.6114. Cited on page 2.

[2] FCC Collaboration, *FCC-ee: The Lepton Collider*, The European Physical Journal Special Topics **228** (2019) 261–623. Cited on pages 3, 5, 6, 8, and 9.

[3] E. Berger, et al., *CLIC CDR - physics and detectors: CLIC conceptual design report.*, https://www.osti.gov/biblio/1035023. Cited on page 3.

[4] T. Behnke, et al., *The International Linear Collider Technical Design Report*, tech. rep., Geneva, 2013. arXiv:1306.6329. Cited on page 3.

[5] The CEPC Study Group, *CEPC Conceptual Design Report: Volume 2 - Physics Detector*, 2018. https://arxiv.org/abs/1811.10545. Cited on page 3.

[6] T. Roser, et al., *Report of the Snowmass 2021 Collider Implementation Task Force*, 2022. https://arxiv.org/abs/2208.06030. Cited on page 4.

[7] *The Future Circular Collider*, https://home.cern/science/accelerators/future-circular-collider. last accessed 19.01.2023. Cited on page 5.

[8] *FCC-ee: beyond a Higgs factory*, Jan., 2021. https://cerncourier.com/a/fcc-ee-beyond-a-higgs-factory/. last accessed 19.01.2023. Cited on page 5.

[9] C. Lippmann, *Particle identification*, Nucl. Instrum. Meth. A **666** (2012) 148–172, arXiv:1101.3276 [hep-ex]. Cited on page 7.

[10] ATLAS Collaboration, G. Aad, et al., *Configuration and performance of the ATLAS b-jet triggers in Run 2*, Eur. Phys. J. C **81** (2021) 1087, arXiv:2106.03584. Cited on page 8.

[11] N. Bacchetta, et al., *CLD – A Detector Concept for the FCC-ee*, 2019. https://arxiv.org/abs/1911.12230. Cited on page 8.

[12] RD-FA Collaboration, M. Antonello, *IDEA: A detector concept for future leptonic colliders*, Nuovo Cim. C **43** (2020) 27. Cited on page 8.

[13] Particle Data Group Collaboration, R. L. Workman and Others, *Review of Particle Physics: Passage of Particles Through Matter*, PTEP **2022** (2022) 083C01. Cited on pages 9 and 12.

[14] M. Aleksa, *Noble liquid calorimetry at the LHC and prospects of its application in future collider experiments*, Europhysics News **52** (2021) 28–31. Cited on page 9.

[15] N. Morange, *Noble Liquid Calorimetry for FCC-ee*, Instruments **6** (2022) 55. Cited on page 9.

[16] A. Strandlie and R. Frühwirth, *Track and vertex reconstruction: From classical to adaptive methods*, Reviews of Modern Physics **82** (2010) 1419–1458. Cited on page 11.

[17] T. G. Cornelissen, et al., *Updates of the ATLAS Tracking Event Data Model (Release 13)*, tech. rep., CERN, Geneva, 2007. http://cds.cern.ch/record/1038095. Cited on page 12.

[18] M. Stefano, *Multiple scattering for particles in matter*, https://meroli.web.cern.ch/lecture_multiple_scattering.html. last accessed 19.01.2023. Cited on page 12.

[19] A. Andreazza, *Tracking systems*, 2016. http://www2.fisica.unimi.it/andreazz/AA_TrackingSystems.pdf. last accessed 19.01.2023. Cited on page 13.

[20] G. Borisov and C. Mariotti, *Fine tuning of track impact parameter resolution of the DELPHI detector*, Nucl. Instrum. Meth. A **372** (1996) 181–187. Cited on page 13.

[21] S. Bheesette, et al., *Medipix3RX neutron camera for ambient radiation measurements*, pp. , 1–5. 2017. Cited on page 13.

[22] M. Havránek, et al., *DMAPS: a fully depleted monolithic active pixel sensor—analog performance characterization*, Journal of Instrumentation **10** (2015) P02013. Cited on page 13.

[23] T. Hirono, et al., *Depleted fully monolithic active CMOS pixel sensors (DMAPS) in high resistivity 150 nm technology for LHC*, Nuclear Instruments and Methods in Physics Research Section A: Accelerators, Spectrometers, Detectors and Associated Equipment **924** (2019) 87–91. Cited on page 13.

[24] ALICE Collaboration, F. Reidt, *Upgrade of the ALICE ITS detector*, Nuclear Instruments and Methods in Physics Research Section A: Accelerators, Spectrometers, Detectors and Associated Equipment **1032** (2022) 166632. Cited on page 13.

[25] D. Colella, *ALICE ITS 3: the first truly cylindrical inner tracker*, Journal of Instrumentation **17** (2022) C09018. Cited on page 14.

[26] A. Kluge, *ALICE ITS3 — A bent, wafer-scale CMOS detector*, Nuclear Instruments and Methods in Physics Research Section A: Accelerators, Spectrometers, Detectors and Associated Equipment **1041** (2022) 167315. Cited on page 14.

[27] N. Bacchetta, P. Collins, and P. Riedler, *Tracking and vertex detectors at FCC-ee*, The European Physical Journal Plus **137** (2022) 231. Cited on page 14.

[28] M. Mager, *ALICE ITS3: A next generation vertex detector based on bent, wafer-scale CMOS sensors*, Sept., 2021. https://indico.cern.ch/event/1071914/attachments/2316015/3942587/2021-09-24_DetectorSeminar-ITS3.pdf. last accessed 19.01.2023. Cited on page 14.

[29] G. Ganis, C. Helsens, and V. Völkl, *Key4hep, a framework for future HEP experiments and its use in FCC*, The European Physical Journal Plus **137** (2022) 149. Cited on page 15.

[30] T. Sjöstrand, *Monte Carlo Generators*, pp. , 51–74. 11, 2006. arXiv:hep-ph/0611247. Cited on page 15.

[31] C. Bierlich, et al., *A comprehensive guide to the physics and usage of PYTHIA 8.3*, SciPost Phys. Codebases (2022). Cited on page 15.

[32] D. J. Lange, *The EvtGen particle decay simulation package*, Nuclear Instruments and Methods in Physics Research Section A: Accelerators, Spectrometers, Detectors and Associated Equipment **462** (2001). Cited on page 15.

[33] A. Buckley, et al., *General-purpose event generators for LHC physics*, Physics Reports **504** (2011) 145–233. Cited on page 15.

[34] S. Agostinelli, et al., *Geant4—a simulation toolkit*, Nuclear Instruments and Methods in Physics Research Section A: Accelerators, Spectrometers, Detectors and Associated Equipment **506** (2003) 250–303. Cited on page 15.

[35] J. de Favereau, et al., *DELPHES 3, A modular framework for fast simulation of a generic collider experiment*, Journal of High Energy Physics **2014** (2014) 57. Cited on page 15.

[36] T. Suehara and T. Tanabe, *LCFIPlus: A framework for jet analysis in linear collider studies*, Nuclear Instruments and Methods in Physics Research Section A: Accelerators, Spectrometers, Detectors and Associated Equipment **808** (2016) 109–116. Cited on page 19.

[37] K. Gautam, et al., *LCFIPlus Vertexing Module in FCCAnalyses*, May, 2022. https://indico.cern.ch/event/1159953/contributions/4871528/attachments/2444787/4189097/LCFIPlusFCCAnalyses_PhysPerf16May.pdf. last accessed 19.01.2023. Cited on page 19.

[38] M. Boscolo, et al., *Challenges for the Interaction Region Design of the Future Circular Collider FCC-ee*, in *Proc. IPAC'21*, pp. , 2668–2671. JACoW Publishing, Geneva, Switzerland, 08, 2021. Cited on page 20.

[39] A. Ciarma, *Vertex Detector Adapted for the 10mm Beam Pipe*, July, 2022. https://indico.cern.ch/event/1174798/contributions/4954476/attachments/2477905/4253219/2022-07-11_MDI_newVXD.pdf. last accessed 19.01.2023. Cited on page 20.